

# Visual-spatial dynamics drive adaptive social learning in immersive environments

Charley M. Wu<sup>1,2,3+</sup>, Dominik Deffner<sup>2,4</sup>, Benjamin Kahl<sup>2</sup>, Björn Meder<sup>2,5</sup>, Mark H. Ho<sup>6\*</sup>, and Ralf H.J.M. Kurvers<sup>2,4\*</sup>

<sup>1</sup>Human and Machine Cognition Lab, University of Tübingen, Tübingen, DE

<sup>2</sup>Centre for Adaptive Rationality, Max Planck Institute for Human Development, Berlin, DE

<sup>3</sup>Department of Computational Neuroscience, Max Planck Institute for Biological Cybernetics, Tübingen, DE

<sup>4</sup>Excellence Cluster: Science of Intelligence, Technical University Berlin, DE

<sup>5</sup>Institute for Mind, Brain and Behavior, Department of Psychology, Health and Medical University, Potsdam, DE

<sup>6</sup>Department of Computer Science, Princeton University, Princeton NJ

\*These authors contributed equally to this work

+Corresponding author: charley.wu@uni-tuebingen.de

## ABSTRACT

Human cognition is distinguished by our ability to adapt to different environments and circumstances. Yet the mechanisms driving adaptive behavior have predominantly been studied in separate asocial and social contexts, with an integrated framework remaining elusive. Here, we use a collective foraging task in a virtual Minecraft environment to unify these two fields, by leveraging automated transcriptions of visual field data combined with high-resolution spatial trajectories. Our behavioral analyses capture both the structure and temporal dynamics of social interactions, which are then directly tested using computational models sequentially predicting each foraging decision. These results reveal that individual performance (rather than social cues) drives adaptation of asocial foraging strategies, while also modulating the influence and selectivity of social learning. These findings not only unify theories across asocial and social domains, but also provide key insights into the adaptability of human decision-making in complex and dynamic social landscapes.

Humans have a unique capacity for social learning that differentiates us from other animals<sup>1,2</sup>. We are remarkably flexible in how we learn from others<sup>3–5</sup>, dynamically integrating personal and social information<sup>6–8</sup>, and selectively favoring social learning when our own capabilities seem lacking<sup>9,10</sup>. And while a number of recent studies have begun to bridge individual and social decision-making<sup>7,11–13</sup>, they either assume fixed strategies or arbitrary mixtures of social and asocial learning. Thus, we still know very little about the mechanisms driving adaptation to different environments and circumstances, allowing us to dynamically arbitrate and integrate both asocial and social learning strategies<sup>14–16</sup>.

Historically, research on asocial and social learning has progressed largely independently from one another. Theories of asocial learning typically assume that decision makers operate alone in a vacuum<sup>17,18</sup>, while theories of social learning<sup>19–21</sup> often greatly simplify—or entirely omit—individual learning mechanisms. Early work investigated the trade-off between individual and social learning through the lens of the producer vs. scrounger dilemma<sup>22–25</sup>, assuming either pure individual learning (i.e., producing) or pure social learning (i.e., scrounging)<sup>26</sup>. In this setting, scrounging comes at the cost of reduced opportunities for producing, with any strategy having *frequency-dependent fitness*, meaning one’s performance depends on the ratio of strategies in one’s group. This dynamic is illustrated in Roger’s Paradox<sup>27</sup>, where too many imitators in a group leads to both lower individual and group fitness. While

theoretical models often show that an intermediate balance of social and asocial learners leads to the best outcomes<sup>28,29</sup>, it is still largely unknown how people dynamically negotiate this balance under realistic conditions and how they adapt to different environmental contexts. For instance, whether adaptation is driven by asocial or social cues, and whether these mechanisms operate independently or interactively with one another. Modeling dynamic strategy selection in social contexts is particularly difficult, because the availability and quality of social information constantly changes as result of both individual decisions and group dynamics<sup>30</sup>. Thus, this gap represents both theoretical and empirical challenges, requiring new methods to capture the complex and dynamic nature of human adaptability, which we seek to address in this current study.

Here, we use a collective foraging task programmed in an immersive Minecraft environment (Fig. 1a-d) to study how people adapt their asocial and social learning strategies to different resource distributions (random vs. smooth; Fig. 1e) and to different dynamic contexts (e.g., individual performance and social observations of success). The virtual environment imposes a limited field of view, creating a natural trade-off between allocating visual attention towards individual search or towards peers for social imitation. Using a novel method for automating the transcription of visual field data (Fig. 1c; see Methods), we can identify which participants and which elements of the environment were visible at any point in time.

This allows us to dynamically integrate visual attention with spatial trajectories and foraging decisions, providing a unified framework for studying the drivers of adaptive behavior.

Adaptive mechanisms have been independently studied in both asocial foraging and social learning, however the two approaches have yet to be integrated in a single framework<sup>15</sup>. In asocial foraging, *area-restricted search*<sup>31</sup> (ARS) has been used to describe an adaptive search strategy from species as diverse as bacteria<sup>32</sup> to humans<sup>33</sup>, where the locality of search is modulated by foraging success: rich rewards drive local search, while poor rewards promote increased search distances. Although ARS is able to account for highly adaptive search patterns, it has yet to be integrated with social learning<sup>15</sup> or other asocial mechanisms of predictive reward generalization<sup>34</sup>. Adaptive mechanisms have also been proposed in social settings, based on context-dependent strategies that compare the quality of individual vs. social information<sup>4,9,10</sup>. Enquist et al.<sup>4</sup> proposed two adaptive strategies: a critical social learner that first tries social learning, but switches to individual learning if social learning proves unsatisfactory, and a conditional social learner, that conversely tries individual learning first, but switches to social learning if necessary. While more flexible than strategies with a fixed level of social learning<sup>27</sup>, these approaches still lack an account of the selectivity of social learning with respect to whom to learn from<sup>5,35</sup> and have yet to be integrated with asocial foraging<sup>15</sup> and reward prediction mechanisms<sup>36</sup>. Here, we bridge this gap through integrative behavioral and model-based analyses.

## Goals and scope

By combining visual field analysis with high-resolution spatial trajectories, we provide new perspectives about how asocial and social learning mechanisms complement one another in a dynamic and integrative fashion. Our results show that people dynamically *adapt* asocial and social learning mechanisms to both the environment and individual performance, *specialize* their social attention patterns, and *selectively* direct social learning towards successful individuals (Fig. 2). Our behavioral analyses capture both the structure and temporal dynamics of social interactions (Fig. 2-3), which are then directly tested using computational models sequentially predicting each foraging decision (Fig. 4). Our winning model integrates adaptive mechanisms of asocial and social learning under a unified framework, revealing that individual success (rather than social factors) drives changes in asocial foraging patterns and increases both the influence and selectivity of social learning.

## Results

Participants ( $n = 128$ ) foraged for hidden rewards either alone or in groups of four (solo vs. group; within-subject) in a virtual environment with  $20 \times 20$  resource blocks (Fig. 1a-d). We manipulated the reward distribution (random vs. smooth) to modify the value of social learning (Fig. 1e). Smooth environments had clustered rewards, making social observations

of successful individuals (visible as a blue splash; Fig. 1b) predictive of other rewards nearby. In contrast, random environments offered unpredictable rewards providing no benefits for social learning. Agent-based simulations (see Methods) confirm this intuition, with asocial learners dominating in random environments, whereas selective, success-biased social learners performed best in smooth environments (Fig. 1f). Thus, peers can be valuable sources of social information (in smooth environments) but also competitors for the same limited resources<sup>3,37</sup> (Fig. S1), creating similar real-world dynamics as developing marketplace innovations or engaging in scientific research<sup>38</sup>.

We start by exploring the influence of the environment and social information on behavioral patterns (Fig. 2a-c). Yet, only by analyzing the effects of network structure (Fig. 2d-f) and the temporal dynamics of social interactions (Fig. 2g-i) are we able to reveal the drivers of adaptive asocial and social learning. Next, we analyze social influence events (“pulls”) to ground our analyses in concrete leader-follower dynamics (Fig. 3). Finally, we use computational models predicting sequential foraging decisions to directly test for different combinations of adaptive individual and social learning mechanisms (Fig. 4), integrating the rich spatial and visual dynamics of the task. All results are compared to an asocial baseline, allowing us to specify which mechanisms are uniquely social phenomena.

## Behavioral results

To compare solo and group conditions, we first computed the normalized reward rate (dividing reward rate by expected reward probability of remaining blocks; Fig. 2a) in order to control for faster reward depletion with more people searching for the same number of finite rewards (see Fig. S1). Using a hierarchical Bayesian regression (see Methods), we find that participants acquired greater rewards in smooth environments (posterior mean: 0.22, 95% Highest Density Interval: [0.19, 0.24]), with no influence of social condition (0.002 [-0.02, 0.02]) nor interaction between condition and environment (-0.02 [-0.05, 0.01]). Thus, both individuals and groups achieved higher foraging success in smooth environments.

We then computed the average pairwise distance between participants across conditions (Fig. 2b). In solo rounds, the four participants foraged on separate but identical fields, allowing us to calculate pairwise distances “as-if” they were on the same field. This analysis revealed closer foraging proximity in smooth than in random environments (-0.6 [-0.8, -0.4]; Fig. S2a). Comparing group to solo rounds, participants socially distanced themselves in groups by actively avoiding each other in random environments (0.3 [0.1, 0.5]), but not in smooth environments (0.004 [-0.2, 0.2]). While there was no aggregate social distancing effect in smooth environments, this does not negate the role of context-dependent changes in social distance, as we show below.

Lastly, we used visual field transcription (see Methods) to measure social visibility as the average number of visi-

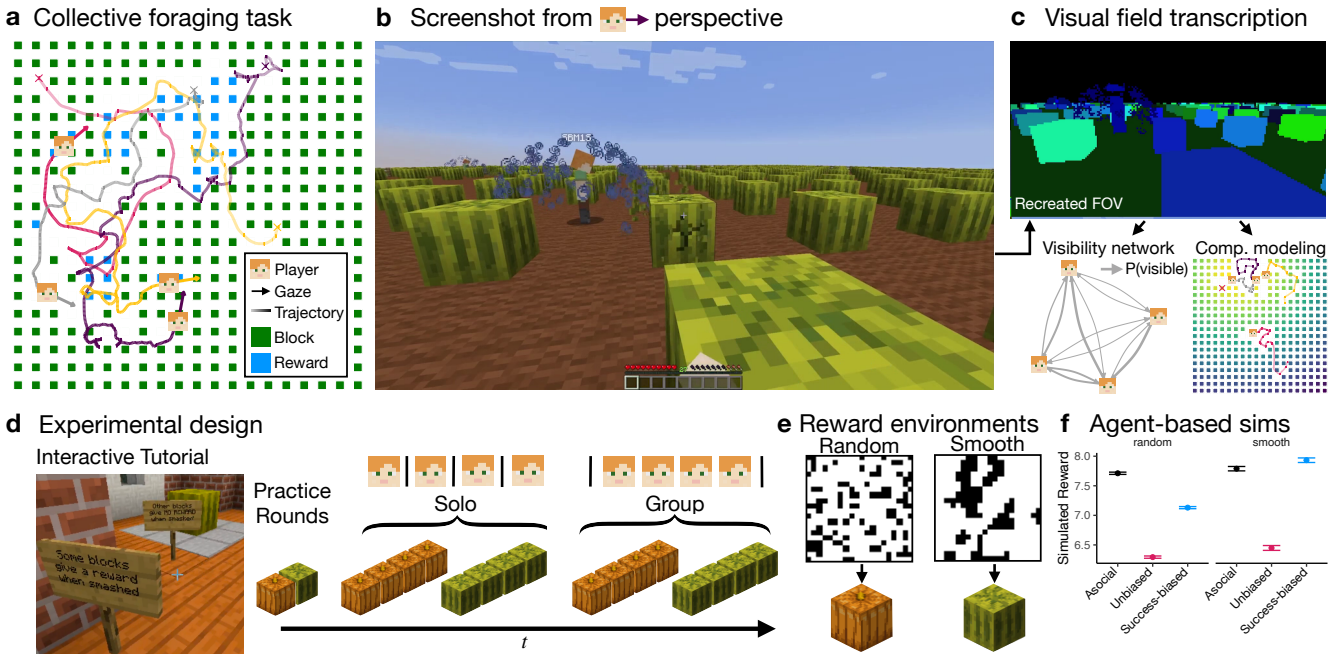


**Figure 1. Collective foraging task implemented in the Minecraft game engine.** (a) Participants foraged for hidden rewards in a field with 20x20 resource blocks. Each round took 120 seconds, with players starting from random locations (crosses) and gaze directions (arrows). (b) Screenshot from a player’s perspective. Rewards (blue splash) are visible to other players, providing relevant social information for predicting nearby rewards in smooth—but not random—environments (Panel e). (c) Automated transcription of each player’s field of view (FOV) used in visibility and model-based analyses (see Methods). (d) Participants learned about the task in an interactive tutorial (Supplementary Video 1) before completing two practice rounds. The main experiment consisted of 16 rounds (counterbalanced order), manipulated across condition (solo vs. group) and reward structure (random vs. smooth) with four consecutive rounds of the same type (Supplementary Videos 2–4). (e) Random environments had uniformly sampled rewards, while smooth environments had spatially clustered rewards. Each black pixel indicates a reward from a representative sample, with both environments having the same base rate  $p(\text{reward}) = .25$ . The mapping to pumpkins and watermelons were counterbalanced between sessions. (f) Agent-based simulations (see Methods) show a benefit for success-biased social learning over asocial learning in smooth, but not random environments, whereas unbiased social learning performs poorly in both.

ble peers (or observers, equivalently) at a given time point (Fig. 2c), again treating solo rounds “as-if” they were on the same field. Participants observed one another more in smooth environments (0.01 [0.001, 0.02]; Fig. S2b), but with no reliable difference between group and solo conditions (-0.0001 [-0.01, 0.01]). In random environments however, participants observed each other less in group vs. solo rounds (-0.01 [-0.02, -0.0005]). Thus, participants actively reduced social attention in random environments (compared to the asocial baseline). Note that at this aggregate level, inbound and outbound social visibility are equivalent, masking individual differences and context-dependent adaptation. We now turn to network analyses to provide a better understanding of the structure and asymmetries of social interactions.

#### Proximity and visibility networks

Next, we performed social network analyses on spatial and visual interactions (Fig. 2d). *Proximity networks* describe each participant as a node with undirected edges weighted by the average proximity (i.e., inverse distance) between play-

ers. *Visibility networks* were constructed similarly, but with directed edges weighted proportional to the duration of time each target player was visible to another player. The same analyses were also applied to solo rounds “as-if” participants had been on the same field.

We first used the proximity network to compute the Eigenvector centrality for each participant, providing a holistic measure of the influence each node exerts on the network. Higher centrality corresponds to participants who maintain close proximity to others, especially to those with high proximity scores themselves. Whereas high centrality tended to correspond to low rewards in random environments (group: -7.6 [-16.6, 0.6]; solo: -7.6 [-16.1, 0.8]; all slopes overlap with 0), we found a robust inversion in smooth environments, where centrality predicted higher rewards in group rounds (7.9 [1.6, 14.0]; Fig. 2e). This effect disappeared in the asocial baseline (2.6 [-5.6, 10.1]), suggesting that the benefits of spatial centrality were due to social dynamics. However, it is unclear whether being central facilitated better performance (via access to social informa-

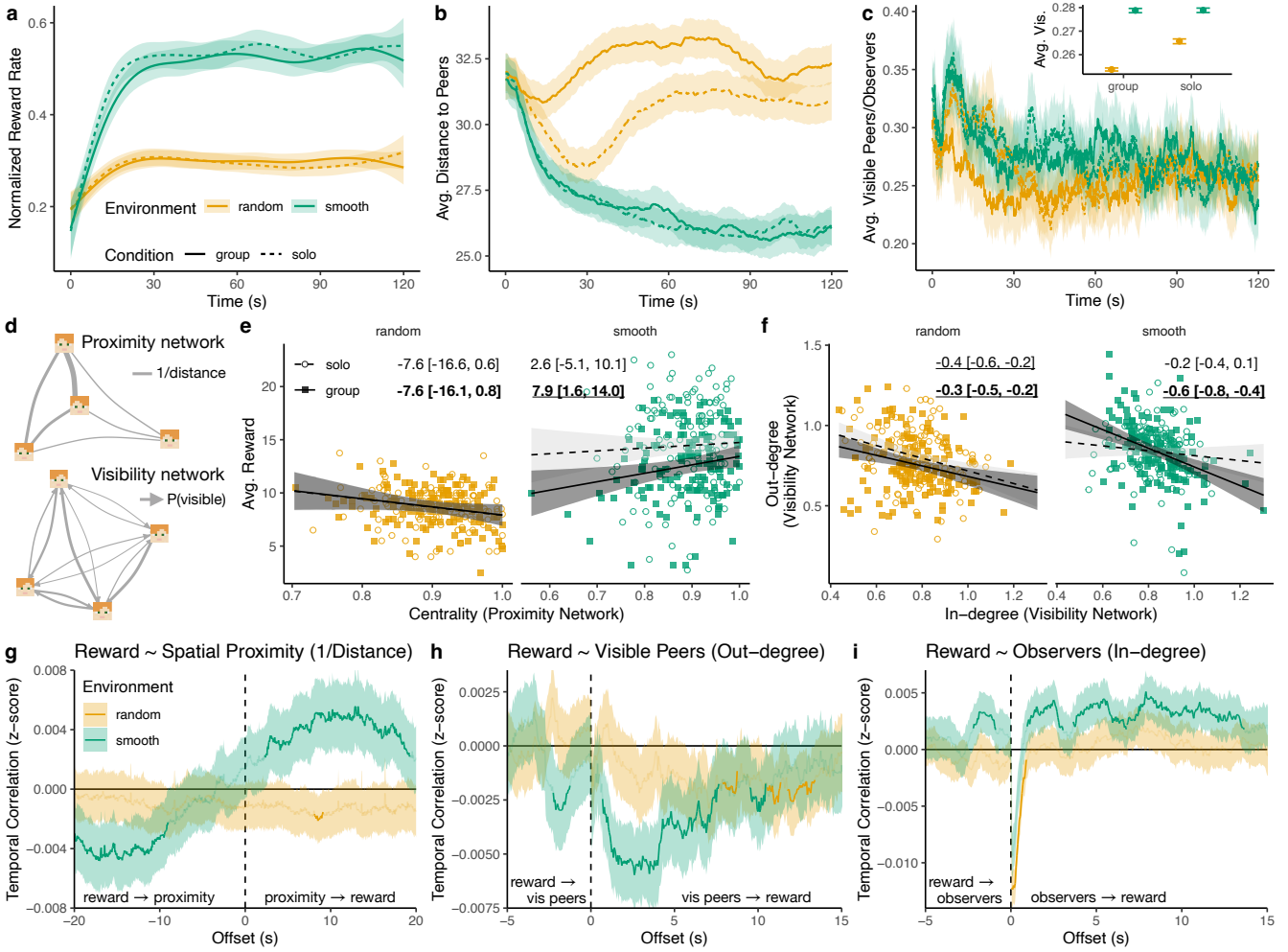


**Figure 2. Behavioral results.** (a-c) Influence of the environment (random vs. smooth) and condition (group vs. solo) on reward rate, spatial distance, and social visibility, with lines showing group-level means and ribbons indicating the 95% CI. Panel a reports normalized reward rate to control for reward depletion (see Fig. S1) and uses a generalized additive model (GAM) for smoothing of binary data. Panels b-c show the raw data (see Fig. S2 for regression results), with the inset in panel c showing the raw data marginalized over time. (d-f) Network analyses. Panel d shows examples of proximity and visibility networks. Panel e shows average reward as a function of Eigenvector centrality computed on the proximity network. Each dot represents one participant; lines and ribbons show the fixed effect of a hierarchical Bayesian regression (reported above; group rounds in bold). Reliable effects (not overlapping with zero) are underlined. Panel f shows the correspondence between in- and out-degree of the visibility network. Each dot represents one participant; the regression line is the fixed effect of a hierarchical Bayesian regression (Fig. S3). (g-i) Temporal dynamics of reward rate and proximity/visibility in group rounds (see Fig. S4 for comparison to solo rounds), where the y-axis shows the sign and strength of the correlation (after chance correction). Bold lines indicate significant clusters that survived a permutation analysis. Effects with negative offsets indicate that reward predicts future proximity/visibility, while effects with positive offsets indicate that proximity/visibility predicts future rewards.

tion) or if centrality resulted from better performance (via effective success-biased imitation), motivating the need for dynamic analyses (see below).

Next, we examined the relationship between in- and out-degree in the visibility network. In-degree is the sum of all inbound edge weights, where being observed by more peers and for longer durations both contribute to larger in-degrees. Similarly, higher out-degree corresponds to observing other peers with longer durations. This analysis revealed an asym-

metry in social attention, with a general inverse relationship between in- and out-degree (Fig. 2f). Whereas this asymmetry was also present in random and solo rounds, it was markedly stronger when combining group rounds and smooth environments (group+smooth interaction: -0.49 [-0.89, -0.08]). This suggests an increased specialization of social learning strategies and asymmetry of social attention in settings where social information was useful. Thus, our network analyses provide insights into asymmetric patterns that could not be detected

at the aggregate-level (Fig. 2c). We now analyze temporal dynamics to better understand how social interactions change over time and in response to different contextual factors.

### Temporal dynamics

To analyze the dynamics of social interactions, we searched for temporally predictive clusters relating individual reward to our high-resolution spatial-visual data (Fig. 2g-i; see Methods). More precisely, we computed correlations between time-series at different temporal offsets (with multiple forms of chance correction), where significant clusters (bold lines in Fig. 2g-i) at negative offsets indicate that individual reward predicts future proximity/visibility, while positive offsets indicate that proximity/visibility predicts future rewards.

First, the dynamics of individual reward (i.e., foraging success) and spatial proximity to other players revealed a pattern of *performance-adaptive spatial cycling* in smooth (but not random) environments (Fig. 2g). The negative correlation at offset -20s to -9s (bold line) indicates that poor rewards predicted increased future proximity (i.e., reduced social distance), whereas high rewards predicted decreased proximity. Subsequently, this creates a cyclical pattern, where the positive correlation at offset 2s to 19s indicates that high spatial proximity predicts high future rewards. Crucially, this pattern is distinct from smooth solo rounds (unimodal positive correlations centered at 0s; see Fig. S4), where we computed the same analysis “as-if” participants were on the same field, allowing us to rule out the role of the environment. Thus, participants closed their social distance when unsuccessful, which then translated into higher future rewards. In turn, higher reward rate predicted reduced proximity, creating a cyclical pattern that was unique to the group condition in smooth environments.

Next, we looked at the dynamics of reward and visual field data, where we analyzed the number of visible peers (outbound social attention towards others; Fig. 2h) and the number of observers (inbound social attention; Fig. 2i) at every timepoint. Starting with outbound visibility of peers (Fig. 2h), we found evidence for *adaptive social attention*. Focusing on smooth environments, a negative correlation at offset -2.3s to -1.3s indicates that low reward predicted seeing more peers in the immediate future, while high rewards predicted less visual attention towards others. This indicates adaptive social learning, where poor individual outcomes promote the acquisition of social information. This effect is reversed in the asocial baseline (Fig. S4), providing evidence that it is a distinctly social phenomenon. We also found several negative correlation clusters at positive offsets for both environments, indicating that the opportunity costs for social information acquisition led to lower future rewards. These opportunity cost clusters were different but also present in solo rounds (Fig. S4), suggesting some generic influence of the task structure (i.e., reduced visibility when destroying a block).

Lastly, the dynamics of reward and inbound visibility (number of observers) indicate *success-biased selectivity*, where participants who acquired higher rewards were the target of so-

cial attention, both in the past and long into the future (Fig. 2i). In smooth environments, the positive correlation at offset -2.2s to -1.0s indicates that higher rewards predicted more future observers within a short time period, which was absent in random environments and inverted in the asocial baseline (Fig. S4). The strong dip around offset = 0s is due to the visual dynamics of the task, since the splash animation temporarily obscured the avatar when acquiring a reward. However, more notably, we observed two clusters with positive correlations in smooth environments (1.0s to 3.0s and 3.7s to 13.6s), which were again absent in random environments and inverted in the asocial baseline (Fig. S4). Thus, participants were not only selective in copying individuals who had been successful in the past, they were also able to identify who would be successful in the future (due to the clustered rewards in smooth environments).

In sum, these temporal dynamics reveal how individual performance is the key driver of adaptive mechanisms, driving changes in social distance (Fig. 2g) and social attention—both when (Fig. 2h) and towards whom (Fig. 2i) it is directed. We next relate these social attention processes to social influence events characterized by leader-follower dynamics.

### Social influence and leadership

Inspired by methods used to study collective decision-making in wild baboons<sup>39</sup>, we analyzed the frequency of “pull” events that capture leader-follower dynamics (see Methods). Each candidate event was selected from min-max-min sequences in the pairwise distance between players (Fig. 3a) and then filtered by a number of criteria including strength (change in distance relative to absolute distance) and disparity (one player moves more than the other). After filtering, we detected a total of 537 pull events (see Fig. 3a for an example), where in each event, one player is identified as a *leader* (moved more during  $[t_1, t_2]$ ) and the other as a *follower* (moved more during  $[t_2, t_3]$ ).

We analyzed both solo and group rounds, with solo rounds providing a benchmark for the sensitivity of these analyses by accounting for the influence of the reward structure (Fig. 3b). While random environments saw a reduction in pull events from solo to group rounds (hierarchical Poisson regression: -0.7 [-1.2, -0.1]), smooth environments saw a large increase in pull events from solo to group rounds (1.4 [0.8, 2.0]). These results were robust to different filter thresholds (Fig. S5) and suggest participants not only adapted their degree of social attention (Fig. 2f,h) but also their susceptibility to social influence depending on the relevance of social learning: following others when adaptive (smooth), and actively avoiding others when maladaptive (random).

Next, we computed a leadership index for each participant based on their frequency of being a leader vs. a follower:  $n_{\text{leader}} - n_{\text{follower}}$ , using only smooth group rounds for interpretability. Participants with a high leadership index were observed more (i.e., higher in-degree) and observed others less (i.e., lower out-degree), indicating a high correspondence between our analysis of these non-overlapping aspects of the

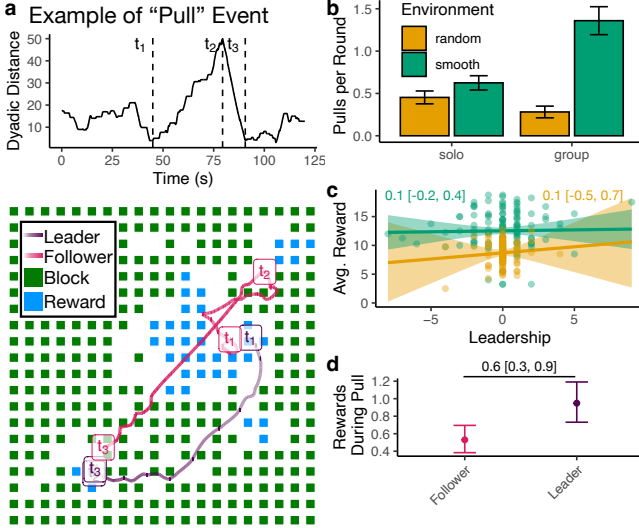


**Figure 3. Social influence.** (a) Example of a pull event, selected from min-max-min sequences in dyadic distance and filtered by a number of criteria (see Methods). The trajectories at the bottom are labeled with the three time points that define a pull, and show the state of the environment at time  $t_3$ . Note that  $t_2$  for the leader largely overlaps with  $t_3$ . (b) The average number of pull events per round ( $\pm 95\%$  CI). We performed the same analysis on solo rounds “as-if” participants were on the same field to provide an asocial baseline. (c) While leadership ( $n_{\text{leader}} - n_{\text{follower}}$ ) did not predict performance, (d) leaders had higher instantaneous rewards during pull events.

data (i.e., visual field data vs. spatial trajectories; see Fig. S6). Yet neither leadership (Fig. 3c) nor in/out-degree predicted performance (Fig. S7f). However, when we focused on the instantaneous reward rate *during* a pull event (Fig. 3d), we found that leaders received more rewards than followers (0.6 [0.3,0.9]). Thus, social influence appears to be modulated by success bias, although we find no long-term benefits of social attention or leadership at the behavioral level, motivating the need for more precise computational modeling (see below).

#### Behavioral summary

Overall, social learning was highly *adaptive* to the environment and depending on individual performance, *specialized* with asymmetry of social attention, and *selectively* directed towards successful individuals and with low out-degree. These behavioral results provide a lens into the dynamics of how asocial and social learning interact and feedback onto each other. However, they only indirectly speak to the individual-level cognitive processes that drive decision making in our experiment. Therefore, we next turn to computational models integrating different combinations of asocial and social learning mechanisms to predict individual foraging decisions.

#### Computational modeling of choices

We use a computational modeling framework (Fig. 4a) to sequentially predict which block participants will destroy next:

$$P(\text{Choice}_{k+1}) \propto \exp(\mathbf{f}_k \cdot \mathbf{w}) \quad (1)$$

Predictions are modeled as a softmax distribution over a linear combination of block features  $\mathbf{f}$  and weights  $\mathbf{w}$ , where we use the state of the world when the  $k$ -th block is destroyed in order to predict the  $k+1$ -th block. Block features  $\mathbf{f}$  capture hypotheses about individual and social learning mechanisms (see below), while weights  $\mathbf{w}$  are estimated using hierarchical Bayesian methods, controlling for individual and group variability as random effects (see Methods).

**Asocial features.** We first used a set of asocial features to capture physical constraints of the task and individual learning through reward prediction (Fig. 4a; see Methods). *Locality* is the inverse distance to the player at time  $k$ , reflecting a tendency to forage locally. *Block Visibility* captures which blocks are within the player’s field of view at time  $k$ , and is set to 1 if visible and 0 if not. *Reward Prediction* uses Gaussian Process regression as a cognitive model of asocial reward generalization in structured environments<sup>34,36</sup>. Since each block can only be destroyed once in each round, reward prediction relies on value function approximation, as a common form of generalization in reinforcement learning<sup>18</sup>, where past observations are used to infer a value function over the search space. Here, we implement this as a binary classification problem, where based on the player’s reward history (until time  $k$ ), we predict the probability of each remaining block containing a reward as a logistic sigmoid of an inferred latent variable  $z$  (Fig. 4a Reward Prediction panel), with higher values corresponding to higher probability of reward (see Methods).

**Social features.** We then incorporate social features based on proximity to different subsets of players. *Successful Proximity* is computed using players who were visible and were observed acquiring a reward (i.e., visible splash) in the span of  $k-1$  to  $k$  (using visual field transcription). We used the last observed location of each player to compute proximity (inverse distance), and use the centroid if there were multiple successful players. *Unsuccessful Proximity* is calculated the same way, but for visible players who were not observed acquiring a reward. In separate models, we also tested *Social Proximity* to all players (irrespective of success) and *Player-specific Proximity*, with unique weights for each target player (see Methods).

#### Model comparison

We compared a series of models, each using a different subset of features. The models fall under one of two classes: *static models* in which the weights remain constant over a round (i.e., fixed strategy), and *dynamic models* in which the weights can change (Fig. 4a bottom left) as a function of the elapsed time since the last individual or socially observed reward (depending on the model):

$$\tilde{\mathbf{w}} = \mathbf{w} + \alpha \cdot \Delta t \quad (2)$$

In dynamic models, the weight estimate  $w$  acts as an intercept, while  $\alpha$  captures the degree of adaptivity as a slope. Since we first normalize  $\Delta t$ , weight estimates are comparable between static and dynamic models. Model comparison is performed separately for group and solo rounds, where we use Bayesian model selection<sup>40</sup> to compute the probability of the best model (i.e., protected exceedance probability; Fig. 4b) and also report individual WAICs relative to the best model (Fig. 4c) for more fine-grained analysis.

Our static models include 1) an *Asocial* model using only asocial features, 2) an *Unbiased* model that adds undifferentiated Social Proximity across all players as a naïve form of social imitation, 3) a *Success-biased* model using separate weights for Successful vs. Unsuccessful players, and 4) a *Player-specific* model with separate proximity weights for each player. Of these models, the Success-biased model performed best in group rounds (Fig. 4c).

Our dynamic models are inspired by influential theories of adaptivity in asocial and social foraging. 5) *ARS* is based on past work using area-restricted search<sup>15,31</sup>, and uses only asocial features, but with the locality weight changing as a function of time since the last individual reward. This corresponds to the common finding that search distance adapts to foraging success<sup>38</sup>, and was the best model in solo rounds and the second best in group rounds (Fig. 4b-c). We also developed two adaptive social learning models inspired by Enquist et al.<sup>4</sup>, both based on our success-biased model. 6) The *Critical learner* adapts the reward prediction weight as a function of time since the last socially observed reward, while 7) the *Conditional learner* adapts both the successful and unsuccessful proximity weights as a function of time since the last individual reward. Thus, the critical learner adapts individual learning as a function of social learning success, while the conditional learner adapts social learning as a function of individual success, with the latter performing better (Fig. 4c). We then combined *ARS* with the *Conditional learner* to create 8) an *ARS+Cond* hybrid, where individual performance drives adaptivity of both asocial (i.e., locality weight) and social (i.e., success-biased imitation) mechanisms. This *ARS+Cond* model vastly outperformed all other models in group rounds ( $p(\text{bestModel}) > .999$ ; Fig. 4b) and was better than the sum of its parts (i.e., *ARS* or *Conditional learning* alone; Fig. 4c).

### Model weights

We focus on interpreting the weights for the best models in each condition (group: *ARS+Cond*; solo: *ARS*), but all models had similar weights for shared features (Figs. S9-S10).

Locality and Block Visibility influenced choices in all conditions, and were typically stronger in random than in smooth environments (i.e., in the absence of reward-predictive cues). The one exception is Locality in solo rounds, with participants foraging more locally in smooth environments (0.9 [0.8, 0.9]). Reward Prediction weights were reliably strong in smooth environments (0.41 [0.38, 0.45]; no difference between group-solo: 0.02 [-0.02, 0.06]), but were null (solo: 0.02 [-0.01, 0.04]) or negligible (group: 0.04 [0.01, 0.07]) in

random environments. Thus, participants adapted individual reward prediction based on the environment, and this mechanism was unaffected by the integration of social information. We also found adaptation in locality weights in all conditions (i.e. *ARS*), with stronger adaptivity in smooth environments (group: -0.91 [-1.05, -0.77]; solo: -0.68 [-0.76, -0.60]) and in the group condition (-0.56 [-0.87, -0.23]). The negative sign corresponds to a reduction of locality as the participant experienced longer durations without individual rewards, consistent with past models of asocial foraging<sup>15</sup>. Our results expand on these previous findings, by showing that adaptation of local search increases (rather than diminishes) in social settings.

Social feature weights (*ARS+Cond* only) show that participants were strongly influenced by successful players in smooth environments (1.0 [0.8, 1.2]), and substantially less in random environments (smooth - random: 0.7 [0.5, 0.9]). However, even in random environments the effect was reliably different from chance (0.29 [0.07, 0.53]), suggesting a persistence of success-biased imitation even in environments where social learning was irrelevant. In contrast, we found no effect of unsuccessful players in neither smooth (0.004 [-0.14, 0.15]) nor random environments (0.10 [-0.07, 0.25]). We also only observe adaptivity in the successful proximity weights for smooth (0.4 [0.2, 0.5]) but not random environments (0.10 [-0.07, 0.25]). Thus, participants increased their reliance on social information as they experienced longer periods without individual reward, with increased selectivity towards successful players.

Altogether, our modeling framework allows us to unify theories of asocial and social adaptation from past literature<sup>4,15</sup>, made possible by our unique combination of visual and spatial data. Here, we show that these adaptive mechanisms are driven by individual performance, and themselves adapt to the context of different reward environments. Furthermore, individual weight and adaptability estimates can also be related to a number of behavioral signatures (Fig. S11-S13), with greater adaptability of locality (more negative estimates) and successful proximity weights (more positive) predicting performance, spatial centrality, and visual attention towards peers.

## Discussion

Collective foraging is a common metaphor for human social learning<sup>38,41,42</sup>. With similar dynamics as marketplace innovation or scientific research, peers can be both useful sources of social information, but also competitors for the same limited resources. Here, we used an immersive virtual environment (Fig. 1), where each individual's limited field of view imposes a trade-off between allocating attention to individual or social learning, while spatial proximity to others directly shapes opportunities (and also costs) for social interactions. With unprecedented access to visual field data (Fig. 1c) and spatial trajectories, our analyses provide unique insights into the structural and temporal dynamics of social interactions, where we study how people adapt to both differ-

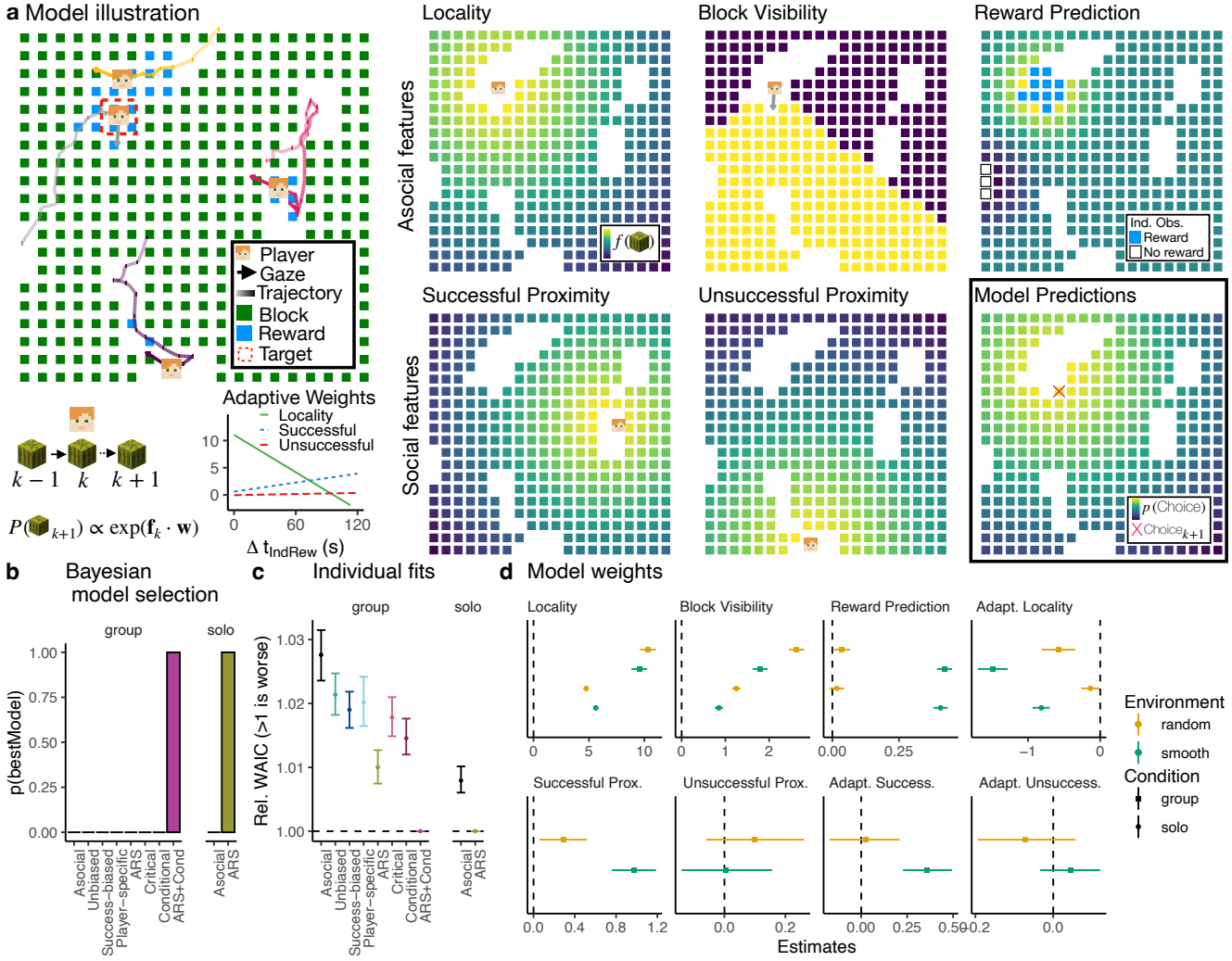


**Figure 4. Computational model.** (a) Left: Model illustration focusing on the player highlighted in the red dashed line. Right: Different models incorporate different sets of features (see text for details), where we illustrate the five features of the winning ARS+Cond model. Increasingly yellow colors correspond to higher feature values, with model predictions (bottom right) shown using the posterior mean of population-level weight estimates, with the red cross indicating the actual choice. ARS+Cond is a dynamic model, where locality and successful/unsuccessful proximity weights (bottom left) change as a function of time since the last individual reward. (b) Model comparison using protected exceedance probability<sup>40</sup> to describe the posterior probability of the best model. (c) Individual model fits showing relative WAICs to the winning model (in each condition), showing the group means (dot) and 95% CIs (error bars). (d) Population-level weight estimates of the best models (group: ARS+cond; solo: ARS; see Figs. S9–S10 for all models), showing the posterior mean (dot) and 95% HDI (lines), with a vertical dashed line at 0.

ent reward environments (smooth vs. random; Fig. 1e) and to dynamically changing social environments.

Our results shed light on the adaptive mechanisms driving collective human behavior, integrating theories from asocial foraging<sup>15</sup> with context-dependent<sup>4,9,10</sup> and selective<sup>5,43,44</sup> social learning. When rewards were smoothly clustered (offering traction for social learning), participants specialized more strongly with greater asymmetry of social attention (Fig. 2f), adaptively sought out social information depending on individual performance (Fig. 2g-h), and selectively

directed their social learning towards successful individuals (Fig. 2i). Participants were also more susceptible to measurable social influence events (“pulls”) in smooth environments (Fig. 3b), which were selectively directed towards individuals with higher instantaneous reward rates (Fig. 3d). Our computational models (Fig. 4) combined spatial and visibility data to account for both asocial and social learning mechanisms, which dynamically adapt over time. Here, the winning model combined area-restricted search<sup>15</sup> with conditional social learning<sup>4</sup> (ARS+Cond), where individual performance

was the key factor driving adaptivity of both local foraging and selective social learning (Fig. 4d). Individual estimates of adaptive local search and success-biased imitation can also be related to better performance, greater spatial centrality, and visual attention towards peers (Fig. S11-S13). Overall, this work integrates previously disparate theories of adaptive mechanisms of asocial and social learning, with their interaction revealing an amplification of adaptivity and selectivity.

## Limitations and future directions

While substantially reduced, success-biased social learning was also present in random environments (Fig. 4d). Thus, despite resources being distributed randomly, participants were still somewhat drawn to successful others, suggesting limitations to the degree of human adaptability and a lingering bias towards social learning. However, even though social information provided no benefits in random environments, it may still offer a computationally cheap tool for engaging in exploration<sup>11</sup> (away from one's current location). Individual exploration is associated with cognitive costs and can be impaired by imposing memory load<sup>45</sup> or time pressure<sup>46</sup>. Thus, social imitation may act as an “exploration device” at a reduced cognitive cost relative to individual exploration<sup>11,47,48</sup>.

The asymmetry of social attention (amplified in smooth environments; Fig. 2f) may act as a safeguard against maladaptive herding<sup>12,49</sup>, where instead of copiers copying other copiers, social learning is selectively directed towards individual learners (low out-degree) and is predictive of successful individuals at long timescales in the future (Fig. 2i). In our study, successful foraging outcomes were made salient by a visual cue (i.e., splash), although people can also deploy metacognitive strategies to infer latent performance or skill from overt behavior<sup>5,14</sup>, providing additional mechanisms for guiding selective social learning. Future work can explore the extent to which these mechanisms (together with our ability to discount correlated social information<sup>50</sup>) may offer a degree of natural protection against the spread of misinformation<sup>51</sup> and the formation of echo chambers through homophilic social transmission<sup>52</sup>.

Future work may consider using a non-depleting reward environment, where collective coordination can yield additive benefits to individual search<sup>5,53</sup>. Indeed, a better understanding of our ability to cumulatively innovate upon previous solutions over long multi-generational timescales has been a powerful motivating force in social learning research<sup>2,27,54</sup>. Here, we have focused on understanding the temporal dynamics of social learning over short timescales, which produced novel insights into the cognitive mechanisms supporting flexible and adaptive social learning. However, a more complete understanding requires connecting social learning mechanisms observed at short timescales to adaptive outcomes over long, cultural timescales. Our work provides the foundations for this endeavor, by providing new perspectives about the cognitive mechanisms that make people such powerful social learners in dynamic and more realistic contexts.

## Conclusions

In conclusion, our study of collective foraging in an immersive Minecraft environment integrated computer-transcribed visual field data with high-resolution spatial trajectories to provide a unified perspective on the adaptive mechanisms of asocial and social learning. Ultimately, this work advances our understanding of the cognitive mechanisms underlying adaptive learning and decision making in social contexts, and provides the foundation for future investigations in non-spatial domains of social interactions.

## Methods

### Participants and design

Participants ( $n = 128$ ) were recruited from the Max Planck Institute for Human Development (MPIB) recruitment pool in Berlin (82 female;  $M_{\text{age}} = 27.4$ ,  $SD_{\text{age}} = 5.0$ ). The study was approved by the Institutional Review Board of the MPIB (number: A 2019-05) and participants signed an informed consent form prior to participation. Participants received a base payment of €12 plus a bonus of €0.03 per reward, spending approximately one hour and earning on average €17.32 ± 1.02 ( $SD$ ).

Participants completed the task in groups of four. After an in-game tutorial (Supplementary Video 1) and two practice rounds (see below), participants completed 16 2-minute rounds of the task. Using a within-subject design, we manipulated the reward structure (random vs. smooth; Fig. S14) and search condition (solo vs. group). The order of round types was counterbalanced across groups, with four consecutive rounds of the same type (Fig. 1d). The reward structure and search condition for each round was announced prior to the start of each round in an onscreen notification.

The reward structure of a given round was made salient by mapping each reward structure to either pumpkin or watermelon blocks (counterbalanced across groups). In both reward structures, 25% of blocks contained rewards, but rewards were either randomly or smoothly distributed. The smooth environments were generated by sampling from a Gaussian process<sup>55</sup> prior, where we used a radial basis function kernel (Eq. 12) with the lengthscale parameter set to 4 (similar to<sup>36</sup>). Sampled reward functions were then binarized, such that the top quartile (25%) of block locations were set to contain rewards. We generated 20 environments for both smooth and random conditions (Fig. S14), with each session (i.e., group) subsampling 1 (practice) + 8 (main task) = 9 environments of each class with pseudorandom assignments that were pregenerated prior to the experiment. In the tutorial (Fig. 1d), participants were given verbal descriptions of each reward condition, saw two fully revealed illustrations of each environment class from a bird's-eye perspective, and interactively destroyed a 3x3 patch of both smooth and random environments (Supplementary Video 1).

The search conditions were made salient by having participants stand on a teleportation block either by themselves (solo) or with the other three participants (group) in order to

begin the round. In the solo condition, participants searched on identical replications of the same environments but without interacting with each other. In the group condition, participants searched on the same environment and could interact with, compete against, and imitate one another.

## Materials and procedure

The experiment was implemented as a computer-based experiment, with each computer connected to a modified Minecraft server (Java edition v.1.12.2). The task was originally designed to also allow for data collection in VR using the Vivecraft mod, which could be done seamlessly by having a participant use a VR headset instead of a mouse and keyboard, without any modifications to the experiment. However, preliminary testing revealed that locomotion via teleportation (the preferred method to avoid VR motion sickness) resulted in less naturalistic spatial trajectories and also interfered with the visual field analyses due to the field of view temporarily fading to black during movement. In contrast, the computer-based modality captured naturalistic trajectories in both space and gaze direction.

In the experiment, the sound was turned off, participants could not see each other's screens, and task-irrelevant controls (e.g., jumping, sprinting, inventory, etc...) were made unavailable. The Minecraft world consists of "blocks" that can be "mined" for resources by holding down the left mouse button to hit them until they are destroyed. In the experiment, participants controlled an avatar that moved through our custom-made environment, defined as a flat field containing a 20x20 grid of 400 pumpkin or watermelon blocks (Fig. 1a) with a two block space between each block. The field was bounded by an impassable fence. See Supplementary Video 2 for a bird's-eye illustration of a round, and Supplementary Videos 3 and 4 for screen captures from group rounds on smooth and random reward environments, respectively.

Each resource block (either watermelon or pumpkin) could be foraged by continually hitting it for 2.25 seconds until it was destroyed, yielding a binary outcome of either reward or no reward. Rewards were indicated by a blue splash effect, visible by other players from any position if it was in their field of view. Only resource blocks could be destroyed in the experiment and destroyed block were not renewed. Blocks did not possess any visual features indicating whether or not they contained a reward. However, rewards in smooth environments were predictable, since observing a reward predicted other rewards nearby. Participants were individually incentivized to collect as many rewards as possible, which were translated into a bonus payment at the end of the experiment. The cumulative number of rewards (reset after the practice rounds) was shown at the bottom of the screen.

After receiving verbal instructions, participants completed an in-game tutorial to familiarize themselves with the controls, how to destroy blocks, the difference between smooth and random reward distributions, and the overall task structure (Supplementary Video 1). They then completed one solo

practice round in a smooth environment and one solo practice round in a random environment. These were identical to the solo condition of the main task, but performance in these rounds did not contribute to a participant's bonus payment. Each round lasted 120 seconds, with the end of the round corresponding to the sun setting below the horizon. This served as an approximate in-game timer for each round, and was communicated to participants in the tutorial. A 3-second countdown timer was also shown onscreen. At the end of the round, participants were given an onscreen announcement indicating the number of rewards they had earned and notifying them of the reward structure and search condition for the next round. Participants were then teleported into a lobby (separate lobbies for solo rounds or a communal one for group rounds), and were required to all stand on a "teleportation" block to indicate readiness for the subsequent round. Prior to the start of a social round, participants all stood on a communal teleportation block, while prior to solo rounds, participants each stood on separate teleportation blocks, in order to induce the social or asocial context. Once all players were ready, a 3-second countdown was displayed and they were teleported into a random position in the next environment with a random orientation direction.

## Data collection

Experimental data was collected using a custom data logging module programmed in Java, which were separated into map logs and player logs. Map logs recorded information about each block destruction event, including a timestamp, player identifier, block position, and the presence or absence of reward. Player logs contained each player's position in the horizontal XZ-plane together with the XYZ components of their gaze vector (i.e., where they were looking). Both logs contained information sampled at Minecraft's native 20 Hz tick-rate (i.e., once every 0.05s), providing high-resolution data about spatial trajectories and gaze directions.

## Automated transcription of visual field data

We developed a custom tool built on the Unity game engine (ver. 2019.3) for performing automated transcription of visual field data (Fig. 1c). We first used data collected from the experiments to simulate each round of the experiment from each participant's point of view. These simulations were then used to automate the transcription of each participant's field of view (Supplementary Video 5).

Our Unity simulations assigned each entity in the experiment (i.e., each block, player, and reward event) a unique RGB value, which was drawn onto a render texture one tenth the size of the player's actual monitor (192x108 pixels as opposed to 1920x1080 pixels). Since the images were rendered without any anti-aliasing or transparency through a simple, unlit color shader, the RGB value of any drawn pixel could be uniquely related with a lookup table to the corresponding entity. We then simulated each round of all experiment data from each player's perspectives within the Unity game engine, using the map logs and player logs, which allowed us to fully

reconstruct the world state. Once all four player perspectives were individually rendered, we could read out the pixels from each player’s field of view, using the RGB colors of the simulated pixels to determine whether an entity was visible at any point in time (20 Hz resolution), and what proportion of the screen it occupied.

In creating these simulations, a few approximations were required. In addition to the reduced resolution mentioned above, player models were approximated by their directionally-oriented bounding box and we ignored occlusion from the heads up display and view-model (e.g., occlusion due to hand position of the avatar). Additionally, some animations produced by the Minecraft game engine include inherent stochastic processes that were approximated. Namely, the splash particles used to indicate a reward event are generated in Minecraft using a random process that spawns 300 particles at predefined locations in a sphere around the player. Whilst the starting locations are deterministic, small deviations in velocity and the lifetime of these particles are generated randomly. Thus, we tuned the parameters of Unity’s particle system to be as authentic as possible by comparing simulated splash effects with video footage of splash effects generated by the Minecraft game engine.

We used a similar procedure for the solo rounds to establish an asocial baseline for our analyses. Whereas all four players searched on different replications of the same field, we simulated them “as if” they were on the same field. Again, a few approximations were required. In these solo simulations, we removed a block whenever any of the four players destroyed it. Additionally, we generated a splash for each reward event, meaning if multiple players foraged the same block in a round, it would trigger a different splash event each time.

### Agent-based simulations

We implemented agent-based simulations to understand how the different reward environments (smooth vs. random rewards) interact with individual-level learning strategies (asocial learning vs. unbiased imitation vs. biased imitation) in determining foraging success (see Fig. 1f). The simulations uses the same features as the computational model, but are defined for a simplified version of the task, capturing the key visual-spatial dynamics of collective decision-making.

More precisely, our simulations modeled the foraging task as a discrete-time sequential game with partial observability, which generalizes Markov decision processes to incorporate multiple agents, partial observability, and separate rewards<sup>56</sup>. Formally, a task is a tuple,  $\langle \mathbb{I}, \mathbb{S}, \mathbb{A}, \mathbb{O}, T, R, O \rangle$ : an agent index set,  $\mathbb{I}$ ; a set of environment states corresponding to configurations of agent locations/directions and available/destroyed blocks,  $\mathbb{S}$ ; a set of joint actions corresponding to agents moving in cardinal directions,  $\mathbb{A} = \times_i \mathbb{A}_i$ ; a set of joint observations,  $\mathbb{O} = \times_i \mathbb{O}_i$ , where each  $\mathbb{O}_i$  is a subset of events viewed from agent  $i$ ’s perspective (i.e., other agents’ locations, reward reveal events, and available blocks); a environment transition function,  $T : \mathbb{S} \times \mathbb{A} \rightarrow \mathbb{S}$ ; a joint reward

function  $R : \mathbb{S} \times \mathbb{A} \times \mathbb{S} \rightarrow \mathbb{R}^{|\mathbb{I}|}$ ; and a joint observation function,  $O : \mathbb{A} \times \mathbb{S} \rightarrow \mathbb{O}$ .

Agents are modeled as selecting a destination to navigate to, navigating to that destination, and then destroying the target block (requiring  $k = 9$  timesteps in the simulation; approximately equivalent to the 2.25 seconds required to destroy a block and the maximum movement speed of 4.3 blocks/second). Agent policies consist of a high-level controller that transitions among different modes of behavior  $n \in \{\text{SelectDest}, \text{NavTo}(x), \text{and forage}(k)\}$ , where  $x$  is a target destination that a low-level navigation controller moves towards and  $k$  is a counter for the number of timesteps left to complete the destruction of a block. When in `SelectDest`, the controller samples a destination from  $P_w(x) \propto \exp\{\mathbf{f}(x) \cdot \mathbf{w}\}$ , where  $\mathbf{f} : X \rightarrow \mathbb{R}^K$  returns a real-valued feature vector (incorporating both asocial and social mechanisms, the same as in the computational models; see below) for each destination block, and  $\mathbf{w} \in \mathbb{R}^K$  are feature weights.

We considered populations of three types of agents. *Asocial agents* used a combination of locality (distance from current location), block visibility (using a 108.5-degree field of view as in the experiment), and asocial reward learning (see the subsection “Gaussian process for binary reward prediction” below). *Unbiased social agents* added an additional feature using the average proximity from observed social partners since the last choice, while *biased social agents* used a similar social proximity feature, but computed only from social partners that were observed acquiring a reward since the last choice. All feature weights were arbitrarily set to 1. For each of 20 random/smooth environments, we generated 100 simulations for each agent type in groups of four agents (for a total of  $20 \times 2 \times 100 \times 3 = 12,000$  simulations). Each simulation was run for 400 timesteps. Figure 1f provides the results of the simulations, showing the average total reward collected by agents by environment type (smooth/random) and strategy (asocial/unbiased social/biased social).

### Hierarchical Bayesian regressions

Statistical analyses were conducted using hierarchical Bayesian regressions to simultaneously model the effects of the experimental manipulations (smooth vs. random and solo vs. group), while controlling for random effects of participants and the group they were assigned to. All regression models used Hamiltonian Markov chain Monte Carlo (MCMC) with a No-U-Turn sampler<sup>57</sup> and were implemented using brms<sup>58</sup>. For count-based variables (e.g., blocks destroyed or pull events), we used Poisson regression, but report the untransformed regression coefficients for simplicity. All models used generic, weakly informative priors  $\sim \mathcal{N}(0, 1)$  and all fixed effects also had corresponding random effects following a maximal random-effects procedure<sup>59</sup>. All models were estimated over four chains of 4,000 iterations, with a burn-in period of 1,000 samples.

## Temporal dynamics

Based on methods developed in Neuroscience<sup>60</sup>, the temporal dynamic analyses (Fig. 2g-i and Fig. S4) use time-series data from each participant in each round to discover temporal structures in social interactions, where rewards predict future spatial/visual patterns and where spatial/visual patterns predict future rewards.

The time-series variables we used are reward (binary vector), spatial proximity (average inverse distance to all other players), and both the number of visible peers and the number of observers (integer variables  $\in [0,3]$ ; acquired from the automated transcription of visual field data) at every point in time (20 Hz time resolution). For solo rounds, we computed both spatial proximity and visibility “as-if” participants were on the same field to provide an asocial baseline.

We then computed correlations between each pair of variables `cor(V1, V2)`, where we iteratively time-lagged V2 from -20 to +20 seconds, with non-overlapping regions of each time series omitted from the data. Each correlation was then *z*-transformed and corrected for chance using a permutation baseline. This chance correction is based on iteratively permuting the order of V2 and computing the correlation `cor(V1, V2_permuted)` over 100 different permutations (for each correlation). We then subtracted the *z*-transformed mean of the permutation correlations from the target correlation. These permutation corrected correlations are reported as a population-level mean ( $\pm 95\%$  CI) in Figure 2g-i and Figure S4.

Lastly, to provide better interpretability of these results, we used a maximum cluster mass statistic<sup>60</sup> to discover temporally continuous clusters of significance at the population level. For each pair of variables [V1, V2] and within each combination of condition (solo vs. group) and environment (random vs. smooth), we used a cluster permutation test to find a threshold for random clusters. This analysis used 10,000 permutations, where for each, we iterated over each individual time series of *z*-transformed (and chance-corrected) correlations, randomly flipping the sign at each time point. We then used a single-sample *t*-test with  $\alpha = .05$  to compute which time points (at the population level) were significantly different from 0. This provided a distribution of the duration of temporally continuous clusters of significance in the randomly permuted data. We then used the upper 95% CI of this distribution as a minimum threshold for the actual data, where we applied the same significance testing procedure, but discarded all clusters shorter in duration than the permutation threshold. The surviving clusters are illustrated with bold lines in Figure 2g-i and Figure S4.

## Social influence

We used methods developed to analyze the movement patterns of geotracked baboons in the wild<sup>39</sup> to measure social influence. This allows us to detect discrete “pull” events over arbitrary time scales, where the movement patterns of one participant (leader) pull in another (follower) to imitate and

forage in the same vicinity (Fig. 3).

We first computed the pairwise distance between all participants (Fig. 3a) and defined candidate pull events from min-max-min sequences, where we used a noise threshold of 1 block distance to determine what corresponds to minimum and maximum distances. These candidate sequences were then filtered based on strength, disparity, leadership, and duration in order to be considered a successful pull.

**Strength**  $S_{i,j}$  defines the absolute change in dyadic distance relative to absolute distance:

$$S_{i,j} = \frac{|d_{i,j}(t_2) - d_{i,j}(t_1)| |d_{i,j}(t_3) - d_{i,j}(t_2)|}{(d_{i,j}(t_1) + d_{i,j}(t_2))(d_{i,j}(t_2) + d_{i,j}(t_3))}, \quad (3)$$

where  $d_{i,j}(t_k)$  is the dyadic distance between participants *i* and *j* at time  $k \in [1, 2, 3]$  (corresponding to the timepoints of the min-max-min sequence). We required pull events to have a minimum strength of  $S_{i,j} > .1$ , such that they correspond to meaningful changes in spatial proximity rather than minor “jitters” at long distance.

**Disparity**  $\delta_{i,j}$  defines the extent to which one participant moves more than the other in each segment, relative to the total distance moved by both participants:

$$\delta_{i,j} = \frac{|\Delta x_i(t_1, t_2) - \Delta x_j(t_1, t_2)| |\Delta x_i(t_2, t_3) - \Delta x_j(t_2, t_3)|}{(\Delta x_i(t_1, t_2) + \Delta x_j(t_1, t_2)) (\Delta x_i(t_2, t_3) + \Delta x_j(t_2, t_3))}, \quad (4)$$

where  $\Delta x_i(t_1, t_2)$  is the displacement between  $t_1$  and  $t_2$ . We filtered pull events to have a minimum disparity of  $\delta_{i,j} > .1$ , such that changes in spatial proximity were asymmetrically driven by one of the interaction partners. Figure S5 shows that our results are robust to changes in the disparity threshold.

**Leadership** is a simple binary filter requiring that the participant who moved more in the first segment ( $t_1$  to  $t_2$ ) moved less in the second segment ( $t_2$  to  $t_3$ ). We refer to the participant who moved the most in the first segment  $\max_{a \in (i,j)} \Delta x_a(t_1, t_2)$  as the *leader* and the participant who moved the most in the second segment  $\max_{b \in (i,j)} \Delta x_b(t_2, t_3)$  as the *follower*. Thus, successful pulls are defined as  $a \neq b$ , where the leader and follower are separate participants.

**Duration** was the final filter, where we required pulls to be at least 3 seconds in duration (since it takes 2.25 seconds to destroy a block). After all filters were applied, the average pull duration was 13.1 seconds  $\pm 0.09$  (SEM).

## Computational modeling

To better understand individual foraging decisions at a mechanistic level, we developed a computational modeling framework that sequentially predicts each block participants destroy based on different combinations of asocial and social features. We modeled the choice probabilities for each block destruction using a linear combination of block features  $\mathbf{f}$  and regression weights  $\mathbf{w}$  that represent the influence of each feature for participants’ block choices (Eq. 1). This was modeled using a categorical likelihood function with  $B_{k+1}$  possible outcomes (i.e., the number of remaining blocks available for

choice at time  $k + 1$ ), with a softmax link function. Different models incorporate different sets of features in  $\mathbf{f}$ , while some dynamic models additionally adapt the weights of specific features as a function of the elapsed time (at time  $k$ ) since the last individually acquired reward or the last socially observed reward (using visual field analysis), depending on the model (see main text).

For interpretability of weight estimates and to allow for identical prior distributions, we  $z$ -standardized all block features within each choice, with the exception of block visibility, which was coded as a binary indicator. We also omitted the first choice in each round, since most features need to be computed with respect to some previous block destruction. Thus, we only started modeling from the second choice in each round, conditioned on the first choice. Furthermore, while all asocial features were included as predictors for each choice, the social features could be undefined for some choices if the conditions were not met (e.g., no visible players, or no visible and successful players). In these situations, the feature values were effectively set to 0 for all blocks.

All model weights were estimated in a hierarchical Bayesian framework with random effects accounting for differences in the importance of (asocial and social) features among individuals and experimental groups. The models were fit using Stan as a Hamiltonian Monte Carlo engine for Bayesian inference<sup>61</sup>, implemented in R v.4.0.3 through cmdstanr version 0.3.0.9. We used within-chain parallelization with `reduce_sum` to reduce model run times through parallel evaluation of the likelihood.

To minimize the risk of overfitting the data, we used weakly informative priors for all parameters. We used weakly informative normal priors centered on 0 for all weight parameters, exponential priors for scale parameters and LKJ priors for correlations matrices<sup>62</sup>. To optimize convergence, we implemented the noncentered version of random effects using a Cholesky decomposition of the correlation matrix<sup>63</sup>. Visual inspection of traceplots and rank histograms<sup>64</sup> suggested good model convergence and no other pathological chain behaviors, with convergence confirmed by the Gelman-Rubin criterion<sup>65</sup>  $\hat{R} \leq 1.01$ . All inferences about weight parameters are based on several hundred effective samples from the posterior<sup>66</sup>. We provide additional details about some model features below.

### **Block visibility**

Since block visibility only captures a static representation of which blocks were visible at time  $k$ , we computed it with permissive assumptions. Specifically, we assumed no object or player occlusions (i.e., object permanence) and used only the horizontal component of their gaze vector to avoid incorporating noise from vertical jitters. Visibility computations used the true horizontal viewing angle of 108.5 degrees, corresponding to the 16:9 aspect ratio monitors used in the experiment.

### **Gaussian process for binary reward prediction**

Gaussian processes<sup>55</sup> provide a Bayesian function learning framework, which we use as a psychological model of reward

generalization for predicting search behavior<sup>36</sup>. Gaussian processes are typically used to learn a function  $f : \mathcal{X} \rightarrow \mathbb{R}^n$  that maps the input space  $\mathcal{X}$  (i.e., the field of destructible blocks) to real-valued scalar outputs, such as continuous reward values.

Here, we modify the Gaussian process framework to the binary classification case, where we want to make probabilistic predictions about whether destroying some block  $\mathbf{x}$  will yield a reward  $p(r = 1|\mathbf{x})$ . This can be described as a logistic sigmoid function  $S(\cdot)$  of some real-valued latent variable  $z$ , such that  $p(r = 1|z) = S(z) = \frac{1}{1 + \exp(-z)}$ . We set the prior mean  $z_0 = \log(\frac{0.25}{1 - 0.25})$  such that  $p(r = 1|z_0) = 0.25$ , corresponding to the true prior probability of rewards. Thus, larger values of  $z$  correspond to higher-than-chance reward probabilities, while lower values correspond to lower-than-chance reward probabilities.

The latent variable  $z$  thus becomes the target of the Gaussian process posterior predictive distribution, computed for some location  $\mathbf{x}_* \in \mathcal{X}$  and conditioned on the past set of observations  $\mathcal{D}_k = \{\mathbf{X}_k, \mathbf{r}_k\}$ :

$$p(r_* = 1|\mathcal{D}_k) = \int p(r_* = 1|z_*) p(z_*|\mathcal{D}_k) dz_* \quad (5)$$

This exact integral in Eq. 5 is analytically intractable, but (i) assuming  $p(z_*|\mathcal{D}_k)$  is Gaussian distributed (using the Laplace approximation<sup>55</sup>; see below) and (ii) approximating  $p(r_* = 1|z_*) = S(z_*)$  with the inverse probit function<sup>67,68</sup>  $\Phi(z_*)$ , we obtain a tractable approximation.

We start by defining a posterior on the latent variable  $z_*$  corresponding to some unobserved block  $\mathbf{x}_*$ :

$$p(z_*|\mathcal{D}_k) = \int p(z_*|\mathbf{z}_k) p(\mathbf{z}_k|\mathcal{D}_k) d\mathbf{z}_k \quad (6)$$

The first term  $p(z_*|\mathbf{z}_k)$  is a Gaussian distribution that can be obtained using the standard GP posterior predictive distribution<sup>55</sup>, while  $p(\mathbf{z}_k|\mathcal{D}_k)$  is intractable. However, the Laplace approximation allows us to approximate the latter term using a Gaussian distribution:

$$p(\mathbf{z}_k|\mathcal{D}_k) = \mathcal{N}(\mathbf{z}_k|\hat{\mathbf{z}}_k, (\mathbf{K} + \mathbf{W} + \sigma_z^2 \mathbf{I})^{-1}), \quad (7)$$

where  $\hat{\mathbf{z}}_k$  is the posterior mode,  $\mathbf{W}$  is a diagonal matrix with diagonal elements  $S(\hat{\mathbf{z}}_k)(1 - S(\hat{\mathbf{z}}_k))$ ,  $\mathbf{K}$  is the  $k \times k$  kernel matrix evaluated at each pair of observed inputs (see Eq. 12),  $\sigma_z^2$  is the noise variance, and  $\mathbf{I}$  is the identity matrix. We set  $\sigma_z^2 = .0001$  as in the environment generating process. The posterior mode  $\hat{\mathbf{z}}$  can be obtained iteratively:

$$\mathbf{z}_k^{new} = \mathbf{K}_z (\mathbf{I} + \mathbf{K}_z)^{-1} (\mathbf{r} - S(\hat{\mathbf{z}}) + \mathbf{W}\hat{\mathbf{z}}_k) \quad (8)$$

where  $\mathbf{K}_z = \mathbf{K} + \sigma_z^2 \mathbf{I}$ ,  $\hat{\mathbf{z}}_k$  is the current estimate of the posterior mode,  $\mathbf{z}_k^{new}$  is the new estimate, and  $\hat{\mathbf{z}}_k = \mathbf{z}_k^{new}$  at convergence.

Eq. 6 can now be derived analytically as a Gaussian  $p(z_*|\mathcal{D}_k) \approx \mathcal{N}(z_*|\mu_{z_*}, \sigma_{z_*}^2)$ , with mean and variance defined as:

$$\mu_{z_*} = \mathbf{k}_*^T (\mathbf{r}_k - S(\hat{\mathbf{z}}_k)) \quad (9)$$

$$\sigma_{z_*}^2 = k(\mathbf{x}_*, \mathbf{x}_*) - \mathbf{k}_*^T (\mathbf{W}^{-1} + \mathbf{K} + \sigma_z^2 \mathbf{I})^{-1} \mathbf{k}_* \quad (10)$$

where  $\mathbf{k}_*$  applies the kernel to the target  $\mathbf{x}_*$  and all previously encountered observations  $\mathbf{k}_* = [k(\mathbf{x}_1, \mathbf{x}_*), \dots, k(\mathbf{x}_k, \mathbf{x}_*)]$ .

Lastly, we use the inverse probit function  $\Phi(z_*)$  as a common method<sup>67,68</sup> for approximating the reward probability as a function of the mean and variance estimates described above:

$$p(r_* = 1 | \mathcal{D}_k) \approx S(\mu_{z_*} (1 + \frac{\pi \sigma_{z_*}^2}{8})^{-1/2}) \quad (11)$$

As a kernel function, we use the radial basis function kernel, which specifies that the correlation between inputs decays smoothly as a function of distance:

$$k(\mathbf{x}, \mathbf{x}') = \exp\left(-\frac{\|\mathbf{x} - \mathbf{x}'\|^2}{2l^2}\right) \quad (12)$$

The degree of smoothness is controlled by the length scale  $l$ , which we set to  $l = \sqrt{48}$ . Note that this is equivalent to the  $l = 4$  used to generate the environments, but accounts for the scaling of the coordinate system in the experiment, where each block has an empty tile on each side.

## References

1. Herrmann, E., Call, J., Hernández-Lloreda, M. V., Hare, B. & Tomasello, M. Humans have evolved specialized skills of social cognition: The cultural intelligence hypothesis. *Science* (2007).
2. Dean, L. G., Kendal, R. L., Schapiro, S. J., Thierry, B. & Laland, K. N. Identification of the social and cognitive processes underlying human cumulative culture. *Science* (2012).
3. Kendal, R. L. *et al.* Social learning strategies: Bridge-Building between fields. *Trends Cogn. Sci.* (2018).
4. Enquist, M. & Ghirlanda, S. Evolution of social learning does not explain the origin of human cumulative culture. *J. Theor. Biol.* (2007).
5. Hawkins, R. D. *et al.* Flexible social inference facilitates targeted social learning when rewards are not observable. *Nat. Hum. Behav.* (2023).
6. Park, S. A., Goiame, S., O'Connor, D. A. & Dreher, J.-C. Integration of individual and social information for decision-making in groups of different sizes. *PLoS Biol.* (2017).
7. Deffner, D., Kleinow, V. & McElreath, R. Dynamic social learning in temporally and spatially variable environments. *Royal Soc. Open science* (2020).
8. Deffner, D. *et al.* Collective incentives reduce over-exploitation of social information in unconstrained human groups. (2023).
9. Morgan, T. J. H., Rendell, L. E., Ehn, M., Hoppitt, W. & Laland, K. N. The evolutionary basis of human social learning. *Proc. Royal Soc. B: Biol. Sci.* (2012).
10. Toelch, U., Bruce, M. J., Newson, L., Richerson, P. J. & Reader, S. M. Individual consistency and flexibility in human social information use. *Proc. Royal Soc. B: Biol. Sci.* (2014).
11. Witt, A., Toyokawa, W., Lala, P., Kevin N, Gaissmaier, W. & Wu, C. M. Flexible integration of social information despite interindividual differences in reward. (submitted).
12. Toyokawa, W., Whalen, A. & Laland, K. N. Social learning strategies regulate the wisdom and madness of interactive crowds. *Nat. Hum. Behav.* (2019).
13. Najar, A., Bonnet, E., Bahrami, B. & Palminteri, S. The actions of others act as a pseudo-reward to drive imitation in the context of social reinforcement learning. *PLoS biology* (2020).
14. Wu, C. M., Vélez, N. & Cushman, F. A. Representational exchange in human social learning: Balancing efficiency and flexibility. (Cambridge University Press, Cambridge, 2022).
15. Dorfman, A., Hills, T. T. & Scharf, I. A guide to area-restricted search: a foundational foraging behaviour. *Biol. Rev.* (2022).
16. Mezey, D., Deffner, D., Kurvers, R. H. J. M. & Romanczuk, P. Visual social information use in collective foraging. (2023).
17. Stephens, D. W. & Krebs, J. R. *Foraging theory*, vol. 1 (Princeton university press, 1986).
18. Sutton, R. S. & Barto, A. G. *Reinforcement learning: An introduction* (MIT press, 2018).
19. Rendell, L. *et al.* Cognitive culture: theoretical and empirical insights into social learning strategies. *Trends cognitive sciences* (2011).
20. Boyd, R. & Richerson, P. J. *Culture and the evolutionary process* (University of Chicago press, 1988).
21. Hoppitt, W. & Laland, K. N. Social processes influencing learning in animals: a review of the evidence. *Adv. Study Behav.* (2008).
22. Barnard, C. J. & Sibly, R. M. Producers and scroungers: a general model and its application to captive flocks of house sparrows. *Animal behaviour* (1981).
23. Vickery, W. L., Giraldeau, L.-A., Templeton, J. J., Kramer, D. L. & Chapman, C. A. Producers, scroungers, and group foraging. *The american naturalist* (1991).
24. Kurvers, R. H. *et al.* The effect of personality on social foraging: shy barnacle geese scrounge more. *Proc. Royal Soc. B: Biol. Sci.* (2009).
25. Mottley, K. & Giraldeau, L.-A. Experimental evidence that group foragers can converge on predicted producer-scrounger equilibria. *Animal Behav.* (2000).

- 26.** Giraldeau, L.-A. & Beauchamp, G. Food exploitation: searching for the optimal joining policy. *Trends Ecol. & Evol.* (1999).
- 27.** Rogers, A. R. Does biology constrain culture? *Am. Anthropol.* (1988).
- 28.** Boyd, R. & Richerson, P. J. Why does culture increase human adaptability? *Ethol. Sociobiol.* (1995).
- 29.** Kameda, T. & Nakanishi, D. Cost–benefit analysis of social/cultural learning in a nonstationary uncertain environment: An evolutionary simulation and an experiment with human subjects. *Evol. Hum. Behav.* (2002).
- 30.** Tump, A. N., Deffner, D., Pleskac, T. J., Romanczuk, P. & Kurvers, R. H. J. M. A cognitive computational approach to social and collective decision-making. *Perspectives on Psychol. Sci.* (2023).
- 31.** Tinbergen, N., Impekoven, M. & Franck, D. An experiment on spacing-out as a defence against predation. *Behaviour* (1967).
- 32.** Macnab, R. M. & Koshland Jr, D. E. The gradient-sensing mechanism in bacterial chemotaxis. *Proc. Natl. Acad. Sci.* (1972).
- 33.** Hills, T. T., Kalff, C. & Wiener, J. M. Adaptive lévy processes and area-restricted search in human foraging. *PLoS One* (2013).
- 34.** Wu, C. M., Meder, B. & Schulz, E. Unifying principles of generalization: past, present, and future. (2024).
- 35.** McElreath, R. *et al.* Beyond existence and aiming outside the laboratory: estimating frequency-dependent and payoff-biased social learning strategies. *Philos. Transactions Royal Soc. B: Biol. Sci.* (2008).
- 36.** Wu, C. M., Schulz, E., Speekenbrink, M., Nelson, J. D. & Meder, B. Generalization guides human exploration in vast decision spaces. *Nat. Hum. Behav.* (2018).
- 37.** Laland, K. N. Social learning strategies. *Learn. & behavior* (2004).
- 38.** Hills, T. T., Todd, P. M., Lazer, D., Redish, A. D. & Couzin, I. D. Exploration versus exploitation in space, mind, and society. *Trends cognitive sciences* (2015).
- 39.** Strandburg-Peshkin, A., Farine, D. R., Couzin, I. D. & Crofoot, M. C. Shared decision-making drives collective movement in wild baboons. *Science* (2015).
- 40.** Rigoux, L., Stephan, K. E., Friston, K. J. & Daunizeau, J. Bayesian model selection for group studies—revisited. *Neuroimage* (2014).
- 41.** Goldstone, R. L. & Ashpole, B. C. Human foraging behavior in a virtual environment. *Psychon. bulletin & review* (2004).
- 42.** Todd, P. M., Hills, T. T. & Robbins, T. W. *Cognitive search: Evolution, algorithms, and the brain*, vol. 9 (MIT press, 2012).
- 43.** Henrich, J. & McElreath, R. The evolution of cultural evolution. *Evol. Anthropol. Issues, News, Rev. Issues, News, Rev.* (2003).
- 44.** Garg, K., Kello, C. T. & Smaldino, P. E. Individual exploration and selective social learning: balancing exploration-exploitation trade-offs in collective foraging. *J. Royal Soc. Interface* (2022).
- 45.** Cogliati Dezza, I., Cleeremans, A. & Alexander, W. Should we control? the interplay between cognitive control and information integration in the resolution of the exploration-exploitation dilemma. *J. Exp. Psychol. Gen.* (2019).
- 46.** Wu, C. M., Schulz, E., Pleskac, T. J. & Speekenbrink, M. Time pressure changes how people explore and respond to uncertainty. *Scientific Reports* (2022).
- 47.** Rendell, L. *et al.* Why copy others? insights from the social learning strategies tournament. *Science* (2010).
- 48.** Toyokawa, W. & Gaissmaier, W. Conformist social learning leads to self-organised prevention against adverse bias in risky decision making. *Elife* (2022).
- 49.** Tump, A. N., Pleskac, T. J. & Kurvers, R. H. Wise or mad crowds? The cognitive mechanisms underlying information cascades. *Science Advances* (2020).
- 50.** Whalen, A., Griffiths, T. L. & Buchsbaum, D. Sensitivity to shared information in social learning. *Cogn. science* (2018).
- 51.** Lewandowsky, S. & Van Der Linden, S. Countering misinformation and fake news through inoculation and prebunking. *Eur. Rev. Soc. Psychol.* (2021).
- 52.** Diaz-Diaz, F., San Miguel, M. & Meloni, S. Echo chambers and information transmission biases in homophilic and heterophilic networks. *Sci. Reports* (2022).
- 53.** Berdahl, A., Torney, C. J., Ioannou, C. C., Faria, J. J. & Couzin, I. D. Emergent sensing of complex environments by mobile animal groups. *Science* (2013).
- 54.** Tennie, C., Call, J. & Tomasello, M. Ratcheting up the ratchet: on the evolution of cumulative culture. *Philos. Transactions Royal Soc. B: Biol. Sci.* (2009).
- 55.** Rasmussen, C. E. & Williams, C. *Gaussian Processes for Machine Learning*. Adaptive Computation and Machine Learning (MIT Press: Cambridge, MA, 2006).
- 56.** Littman, M. L. Markov games as a framework for multi-agent reinforcement learning. In *Machine learning proceedings 1994*, (Elsevier, 1994).
- 57.** Hoffman, M. D. & Gelman, A. The No-U-turn sampler: adaptively setting path lengths in Hamiltonian Monte Carlo. *J. Mach. Learn. Res.* (2014).
- 58.** Bürkner, P.-C. Advanced bayesian multilevel modeling with the r package brms. *The R J.* (2018).

59. Barr, D. J., Levy, R., Scheepers, C. & Tily, H. J. Random effects structure for confirmatory hypothesis testing: Keep it maximal. *J. Mem. Lang.* (2013).
60. Nichols, T. E. & Holmes, A. P. Nonparametric permutation tests for functional neuroimaging: a primer with examples. *Hum. Brain Mapp.* (2002).
61. Carpenter, B. *et al.* Stan: A probabilistic programming language. *J. Stat. Softw.* (2017).
62. Lewandowski, D., Kurowicka, D. & Joe, H. Generating random correlation matrices based on vines and extended onion method. *J. Multivar. Analysis* (2009).
63. McElreath, R. *Statistical rethinking: A Bayesian course with examples in R and Stan* (CRC press, 2020).
64. Vehtari, A., Gelman, A., Simpson, D., Carpenter, B. & Bürkner, P.-C. Rank-normalization, folding, and localization: An improved  $\hat{R}$  for assessing convergence of mcmc. (2019).
65. Gelman, A., Rubin, D. B. *et al.* Inference from iterative simulation using multiple sequences. *Stat. Sci.* (1992).
66. Gelman, A. *et al.* *Bayesian data analysis* (Chapman and Hall/CRC, 2013).
67. Bishop, C. M. Pattern recognition. *Mach. learning* (2006).
68. MacKay, D. J. The evidence framework applied to classification networks. *Neural computation* (1992).
69. Wu, C. M. *et al.* Specialization and selective social attention establishes the balance between individual and social learning. In Fitch, T., Lamm, C., Leder, H. & Teßmar-Raible, K. (eds.) *Proceedings of the 43rd Annual Conference of the Cognitive Science Society*, (2021).

## Data and Code Availability

All data and code for running the experiment, analyzing the data, and the Unity simulations will be made publicly available upon publication.

## Acknowledgements

We thank Philip Jakob for technical support, Philipp Schwartenbeck for advice on cluster correction, and Ariana Strandburg-Peshkin and Damien Farine for publishing their code for analysing pull events. We also thank Ryutaro Uchiyama and Alexandra Witt for helpful feedback on a draft of the manuscript, and Deb Ain for copy editing. CMW is supported by the German Federal Ministry of Education and Research (BMBF): Tübingen AI Center, FKZ: 01IS18039A and funded by the Deutsche Forschungsgemeinschaft (DFG, German Research Foundation) under Germany's Excellence Strategy—EXC2064/1–390727645. RHJMK and DD are funded by the DFG under Germany's Excellence Strategy – EXC 2002/1 “Science of Intelligence” – project number 390523135. A pilot version of this experiment (with different data and design) was presented at the 43rd Annual Conference of the Cognitive Science Society<sup>69</sup>.

## Author contributions statement

CMW and RHJMK conceived the experiment, with feedback from DD, BK, and BM. CMW, DD, BK, and RHJMK performed the experiments. CMW, DD, and MHH analyzed the results. BK developed the visual field transcription method under the supervision of CMW and RHJMK. CMW developed the visualizations and wrote the first draft. All authors reviewed the manuscript.

## Ethics declarations

### Competing interests

The authors declare no competing interests.

# Supplementary Information for Visual-spatial dynamics drive adaptive social learning in im- mersive environments

Charley M. Wu, Dominik Deffner, Benjamin Kahl, Björn Meder, Mark H. Ho, & Ralf H.J.M. Kurvers

## Supplementary Videos

**Movie S1.** Tutorial. The original German text has been translated to English for better interpretability. <https://www.youtube.com/watch?v=QksKYOoElxg>

**Movie S2.** Bird's eye recreation of a group round with smooth rewards. <https://www.youtube.com/watch?v=vUHaAhjfFVo>

**Movie S3.** Screen capture of a group round with smooth rewards (corresponds to Supplementary Video 2). All in-game text was originally in German for all experiments, but have been translated here to English for interpretability. <https://www.youtube.com/watch?v=wyk7RbmHiok>

**Movie S4.** Screen capture of a group round with random rewards. <https://www.youtube.com/watch?v=mWe4CeLWdpq>

**Movie S5.** Automated transcription of visual field using Unity simulations. <https://www.youtube.com/watch?v=iSZ-ewpiZWI>

## Supplementary Results

### Rewards, social distance and foraging rate

Smooth environments resulted in higher rewards in both solo (0.5 [0.4,0.5]) and group conditions (0.3 [0.3, 0.4]; Fig. S1a,c). Within smooth environments, participants performed better in solo than in group rounds (-0.1 [-0.2, -0.1]). However, this effect of solo vs. group condition disappears when we control for faster reward depletion in groups (Fig S1b) by computing normalized reward rate as `rewardRate/expectedRewardRate` (Fig. 2a), where `expectedRewardRate` is the marginal probability that any of the remaining blocks contains a reward. Thus, reward structure is the key driver of performance (Fig S1d).

We then computed the average pairwise distance between participants (Fig. 2b; Fig S2a). Solo rounds provide an asocial baseline by accounting for the influence of reward structure, which we calculated by simulating as if participants were on the same field.

We additionally looked at participant foraging rates, defined as the number of destroyed blocks per second. This analysis revealed greater selectivity in smooth environments, corresponding to a slower rate of blocks destroyed (-0.04, [-0.07, -0.02]; Fig. S2c-d). The selectivity of smooth environments was further amplified in group rounds (-0.03, [-0.06, -0.005]), where participants did not only need to contend with the structure of the environment, but also the structure and dynamics of social interactions.

In sum, smooth environments increased reward rate (Fig. S1a), brought participants closer together (Fig. S2a), and slowed the rate of foraging (Fig. S2c). Groups performed on par with solo rounds when controlling for depletion (Fig. S1d), avoided each other in random environments (Fig. S2a), and foraged slower in smooth environments (Fig. S2c-d).

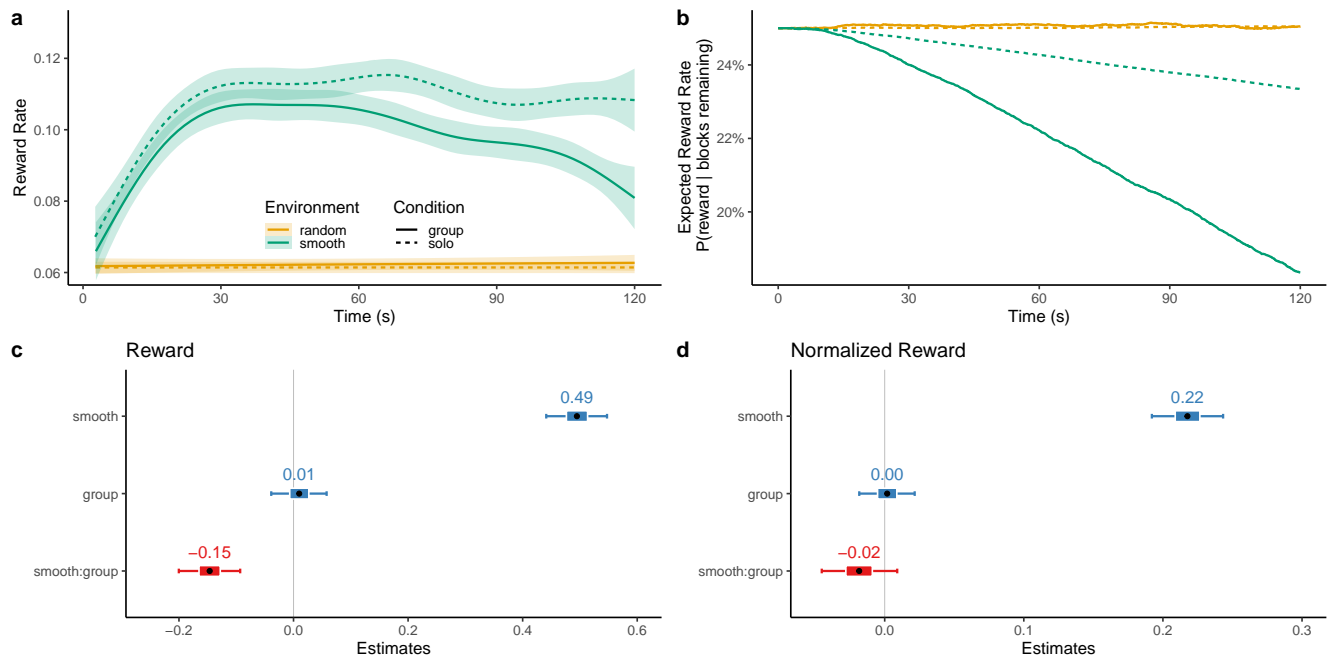


**Figure S1. Reward.** **a)** Smoothed curves showing the average rate of rewards over time as a Generalized Additive Model (GAM). Ribbons indicate 95% CI. **b)** Expected reward rate over time (used to compute normalized reward rate; Fig. 2a), showing the probability that a randomly sampled block (from those remaining) contains a reward. Each line shows the aggregated mean, which only diminished in smooth environments (due to predictable rewards) and much faster in group rounds (due to more participants foraging for the same finite number of rewards). **c)** Coefficient plot of a hierarchical Bayesian Poisson regression showing (un-normalized) rate of rewards. Each dot is the posterior mean and error bars show the 95% CIs. **d)** When running a regression on the normalized rewards, only the effect of smooth environments remains.

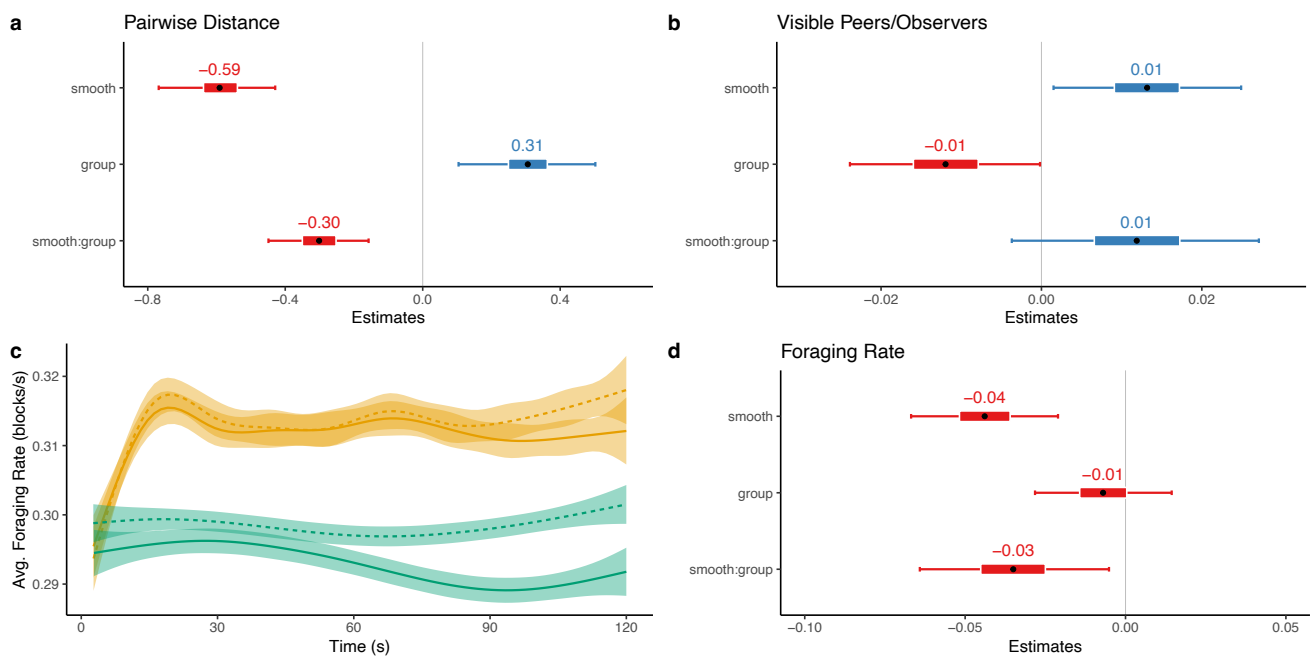


**Figure S2. Pairwise distance and foraging rates.** **a)** Social distance regression coefficients. Participants were closer together in smooth environments and solo conditions. In random environments, participants in groups avoided each other compared to the solo condition. **b)** Visibility regression coefficients. Participants observed each other more in smooth environments, marginally less in the group condition for random, but not smooth environments. **c)** Foraging rate (i.e., the number of blocks destroyed per second) plotted as smooth conditional means. **d)** Regression coefficients. Participants had a lower foraging rate in smooth than in random environments, which was further amplified in group rounds.

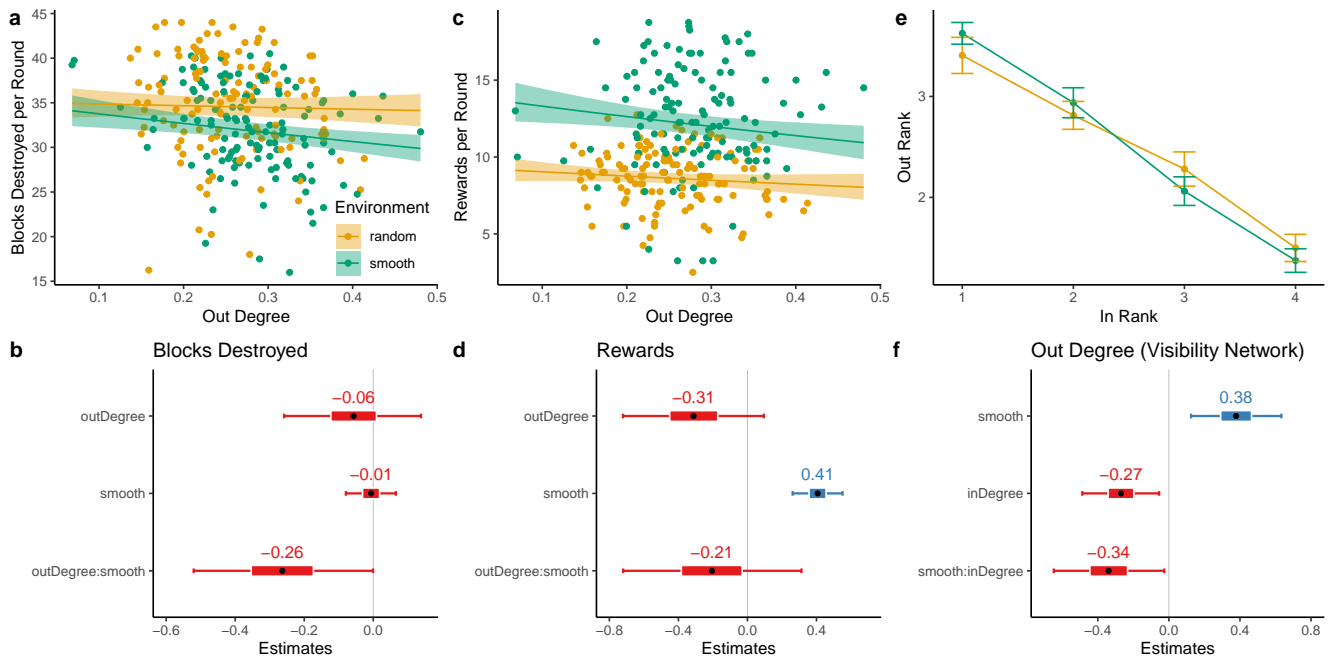


**Figure S3. Relationships between environment, out-degree, in-degree, blocks destroyed and reward rate in groups.**

**a-b)** In smooth environments, participants with a higher out-degree (i.e., observing other players) destroyed fewer blocks (Poisson regression coefficients shown in panel **b**). **c-d)** This did not translate into an effect on the reward rate. **e**) Rank ordering participants in each group according to their in- and out-degree showed a negative correlation between participants' in- and out-degree. **f**) Regression coefficients predicting out-degree. Smooth environments increased out-degree, while higher in-degree decreased out-degree, with a reliably stronger negative effect in smooth environments.

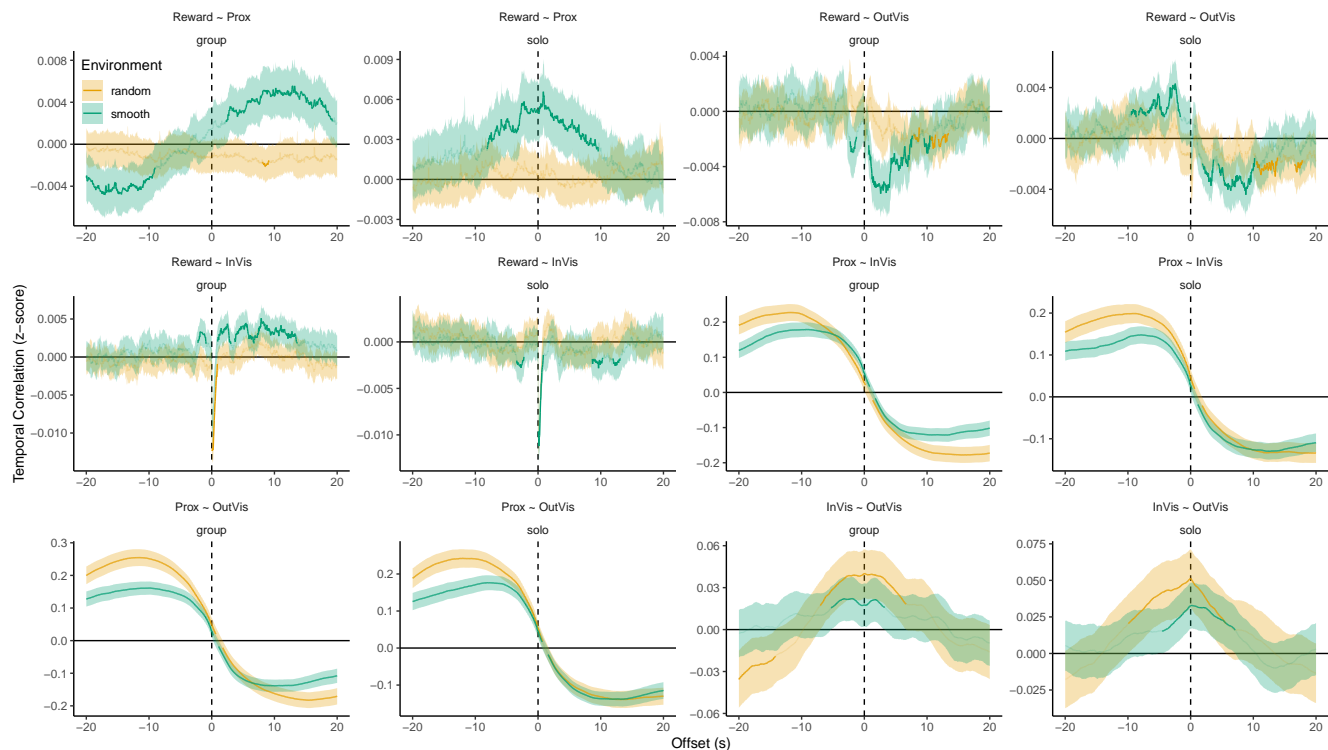


**Figure S4. Temporal dynamics.** Full set of temporal dynamic analyses, including solo rounds. Bold lines indicate significant clusters that survived the permutation analysis (see Methods).

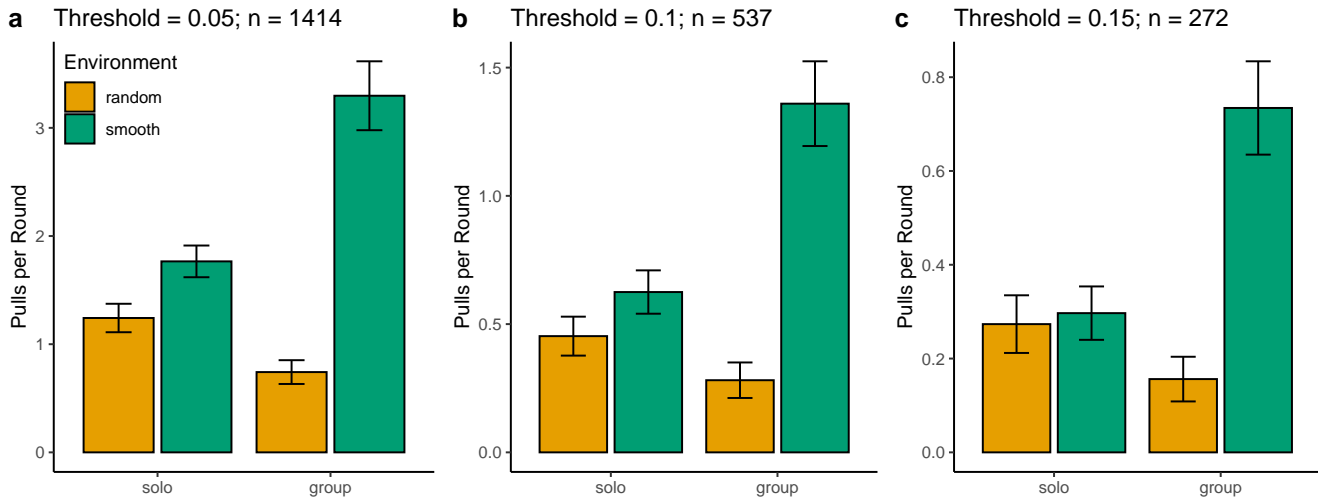


**Figure S5.** Sensitivity analysis of the pull analysis. **a-c**) Independent of the exact disparity threshold used (0.05, 0.1, 0.15; see Methods), the number of pull events decreased from solo to group rounds in random environments, and increased from solo to group rounds in smooth environments.

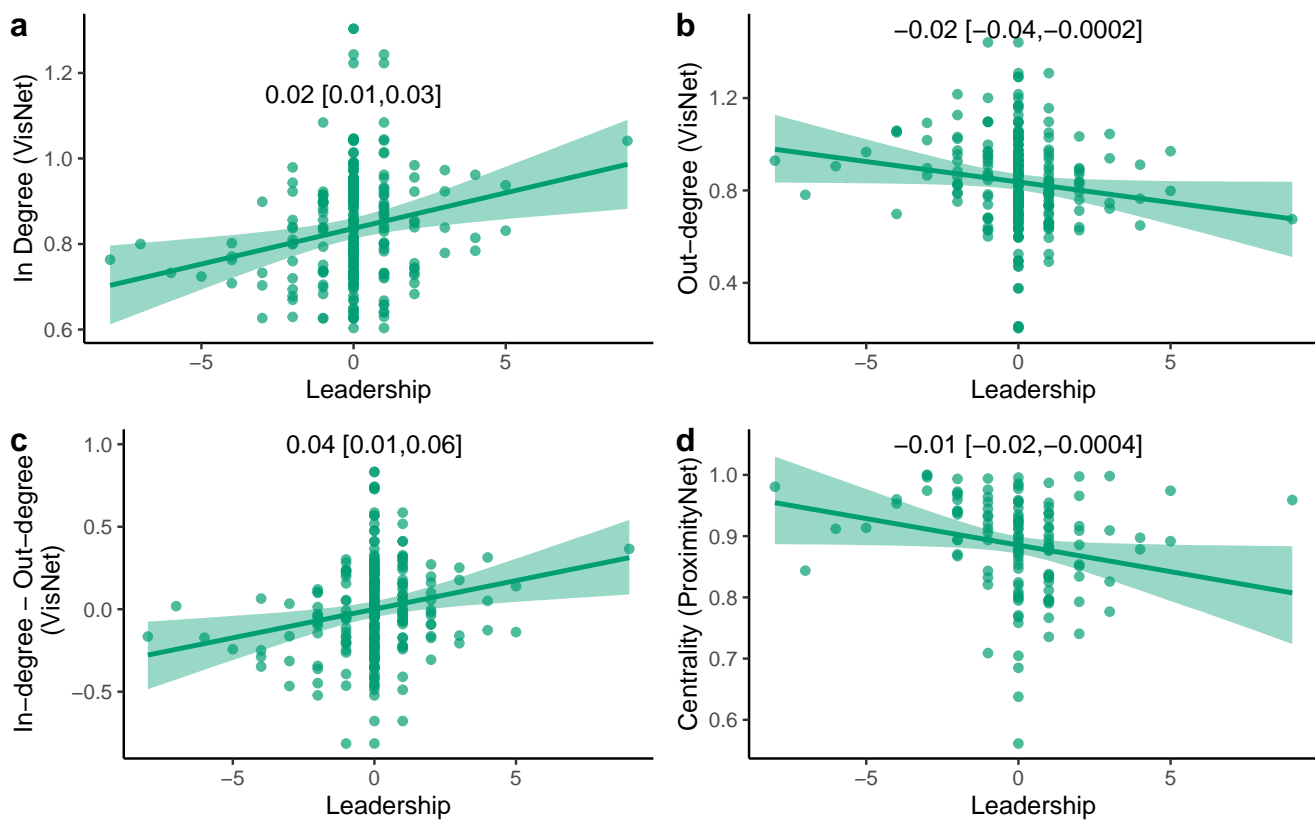


**Figure S6.** Relating leadership to visibility (VisNet) and proximity networks (ProximityNet). Each dot is a participant, with the line (and ribbon) showing the mean ( $\pm 95\%$  CI) of a mixed-effects regression, with the fixed effect reported above. For interpretability, we compute leadership only from group rounds in smooth environments. **a)** Participants with a higher leadership score were observed more (i.e., higher in-degree), and **b)** observed others less (i.e., lower out-degree). **c)** Leadership score also predicted the difference between in-/out-degree, and **d)** high leadership score also predicted lower spatial centrality, suggesting leaders were at the frontiers of the group.

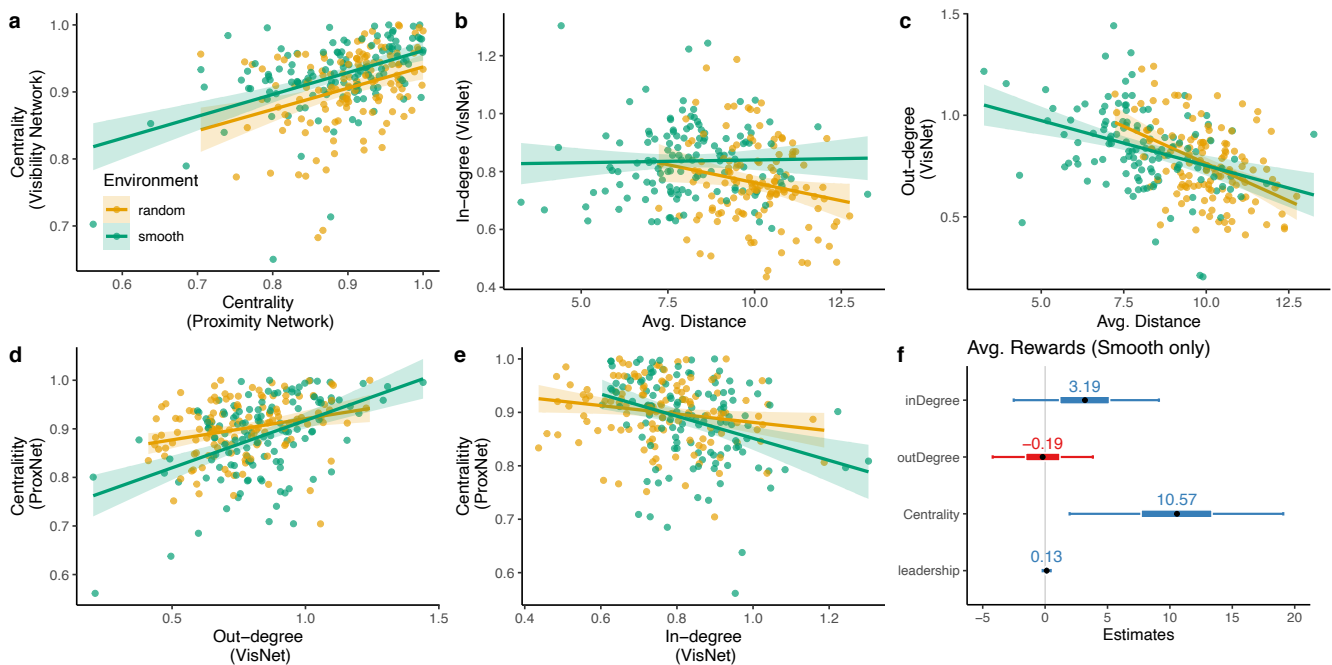


**Figure S7. Consistency of visibility and proximity networks and their relationship to performance (in group rounds).** Each dot is a participant, with the line and ribbon showing a linear regression. **a)** Eigenvector centrality was consistent across visibility and proximity networks. **b)** A player's in-degree was unrelated to their average spatial distance to other players in smooth environments, and negatively correlated in random environments. **c)** Average distance to other players was always negatively correlated to out-degree. **d)** Out-degree was positively correlated with centrality, with a stronger effect in smooth environments. **e)** In-degree was negatively correlated with centrality in both environments. **f)** Bayesian mixed-effects regression predicting the influence of social network statistics on reward (smooth rounds only).

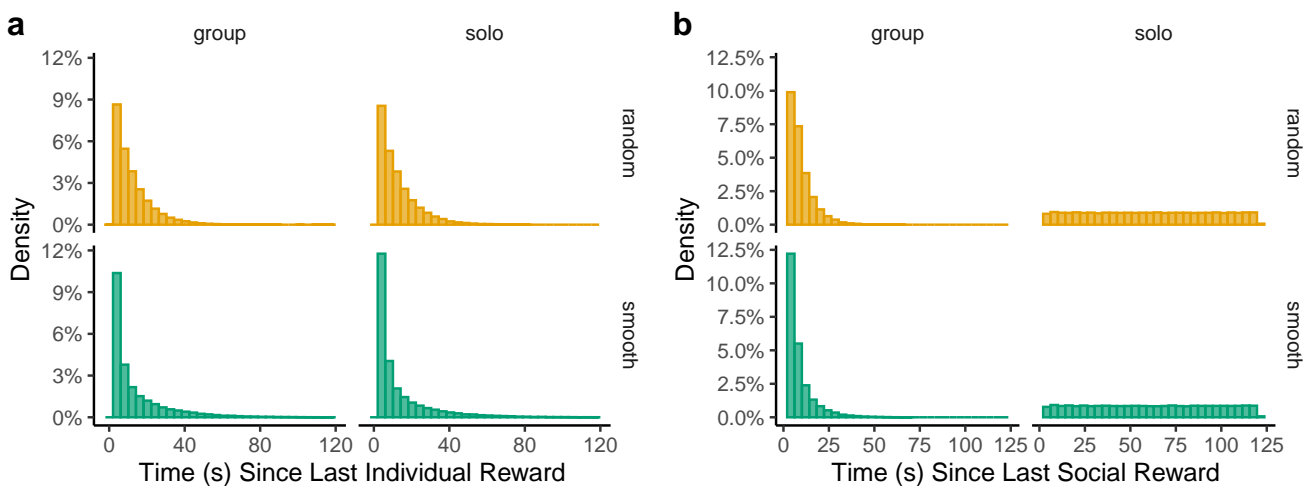


**Figure S8. Histograms of elapsed time between previous individual/social reward events,** computed at each block destruction. These values are used in the adaptive models. Note that solo rounds don't have access to social reward information.

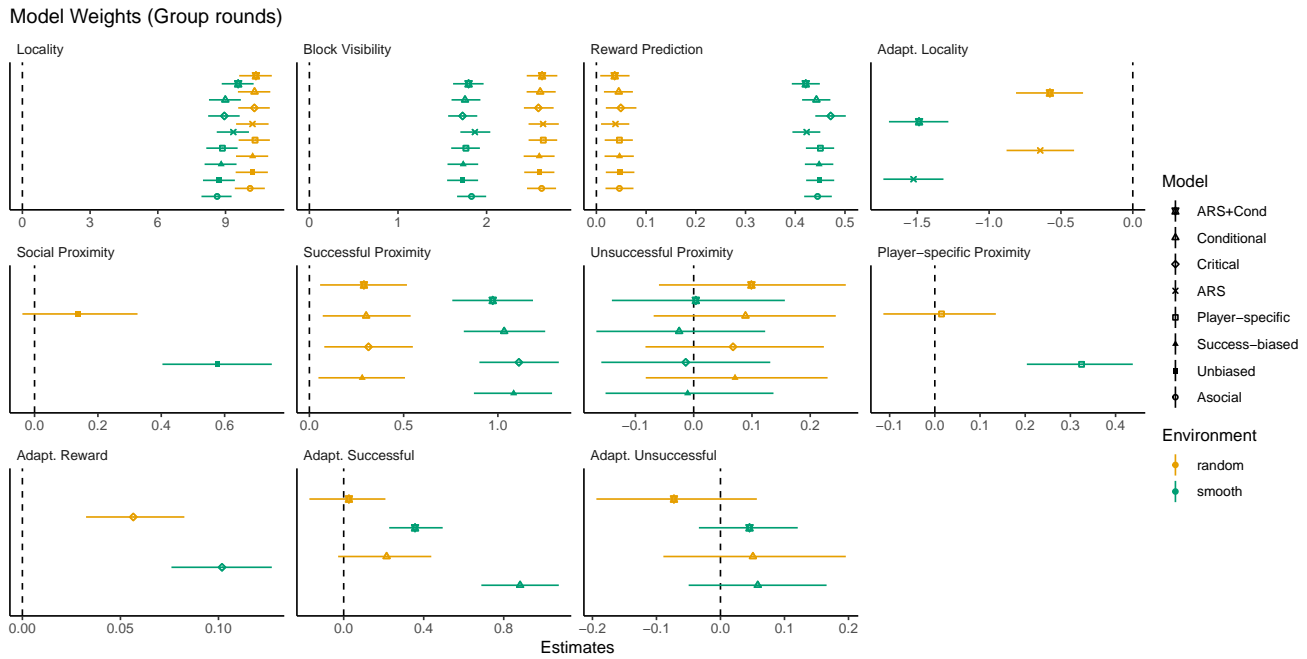


**Figure S9.** Weights for all models in group rounds. Symbols show the posterior mean and error bars the 95% HDI.

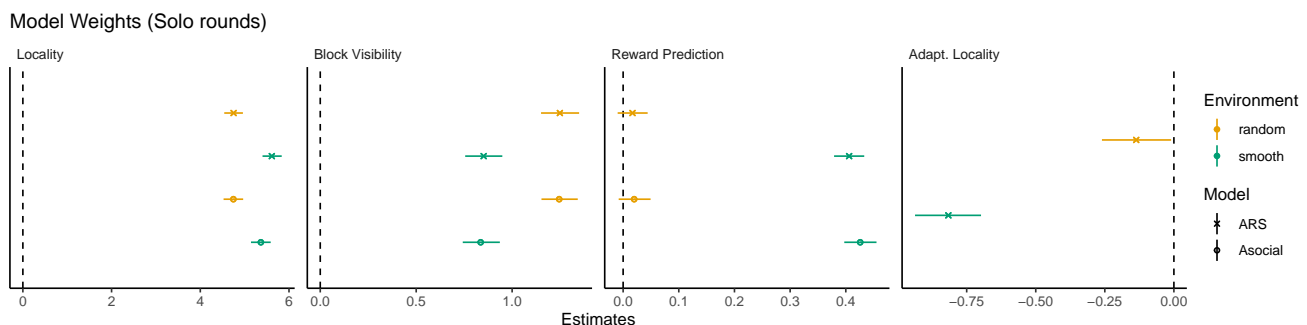


**Figure S10.** Weights for all models in solo rounds. Symbols show the posterior mean and error bars the 95% HDI.

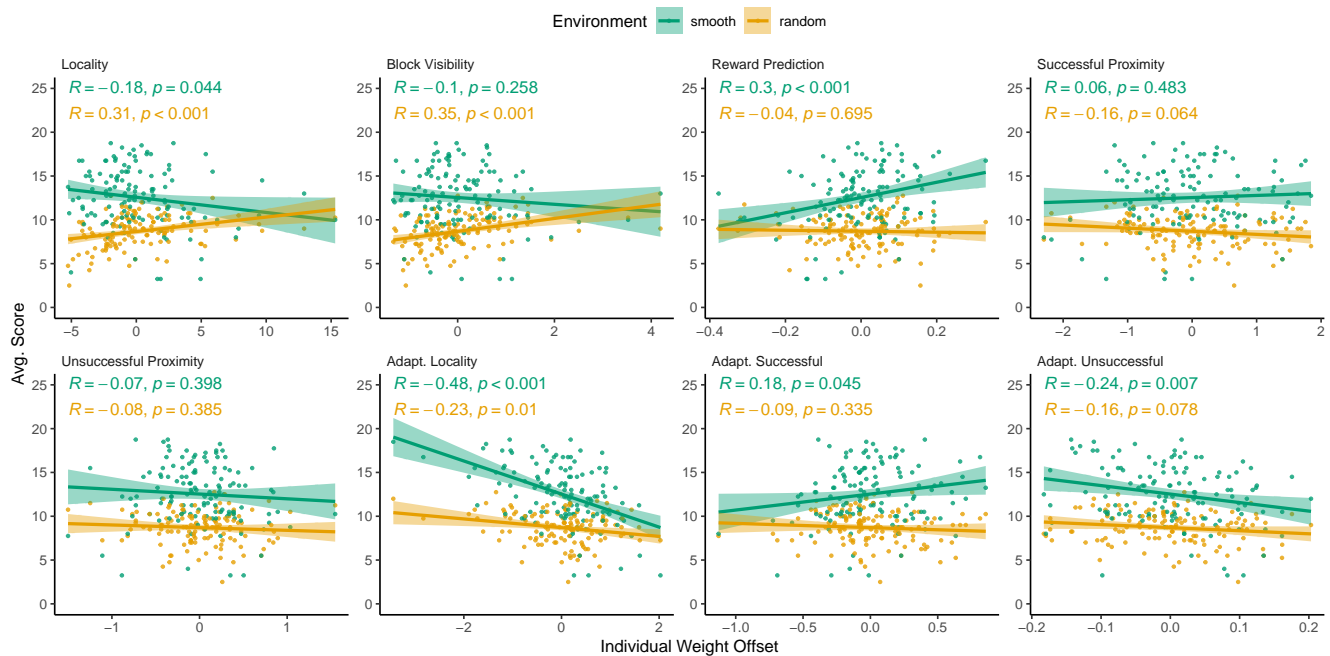


**Figure S11. Individual model and Avg. Score (group rounds).**

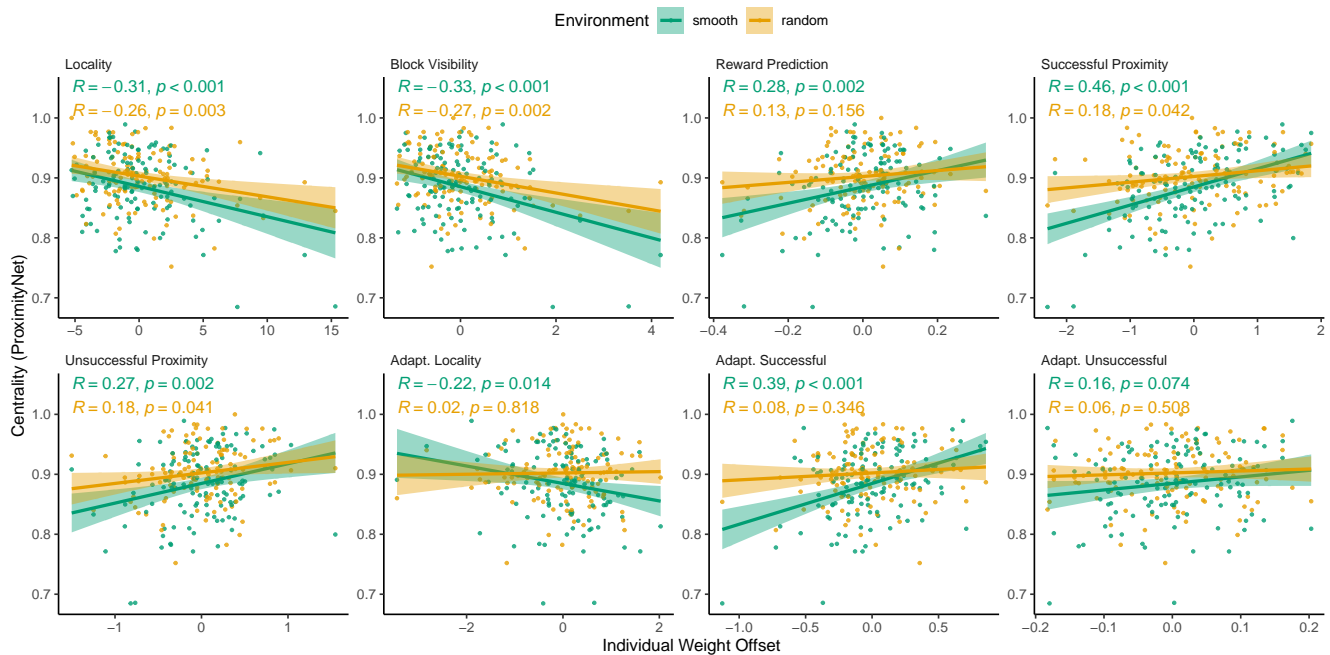


**Figure S12. Individual model weights and spatial centrality (group rounds).**

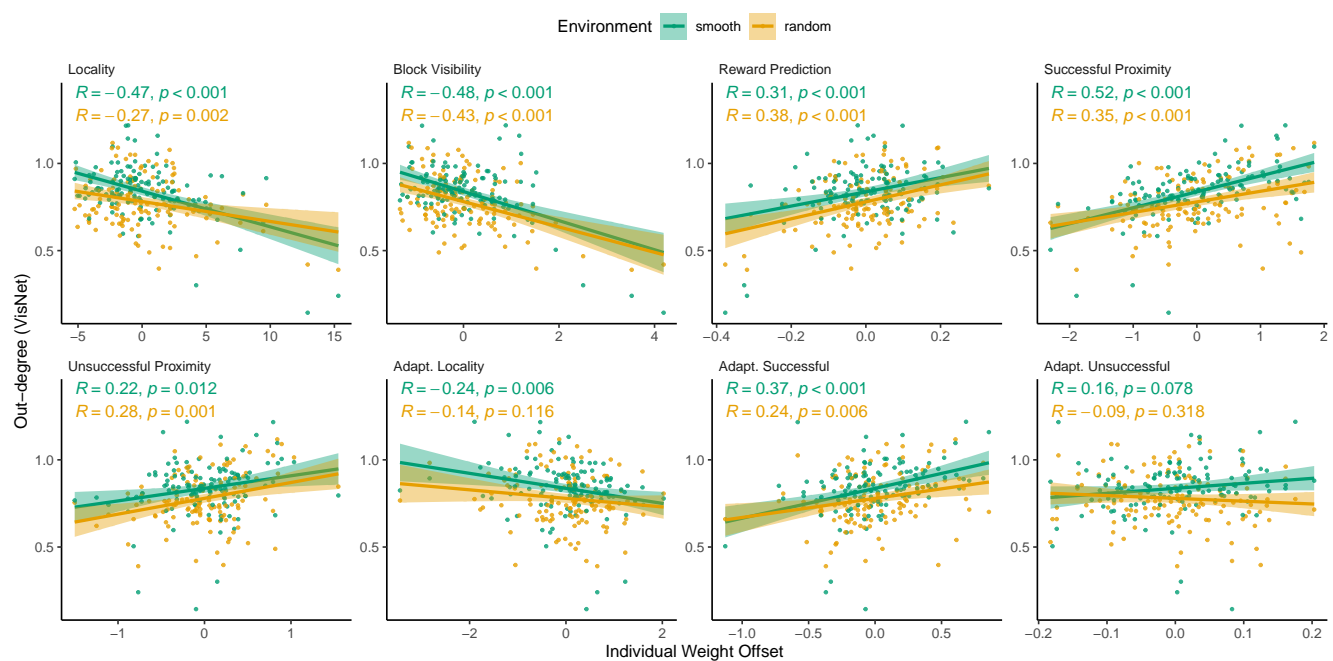


**Figure S13. Individual model weights and out-degree (group rounds).**

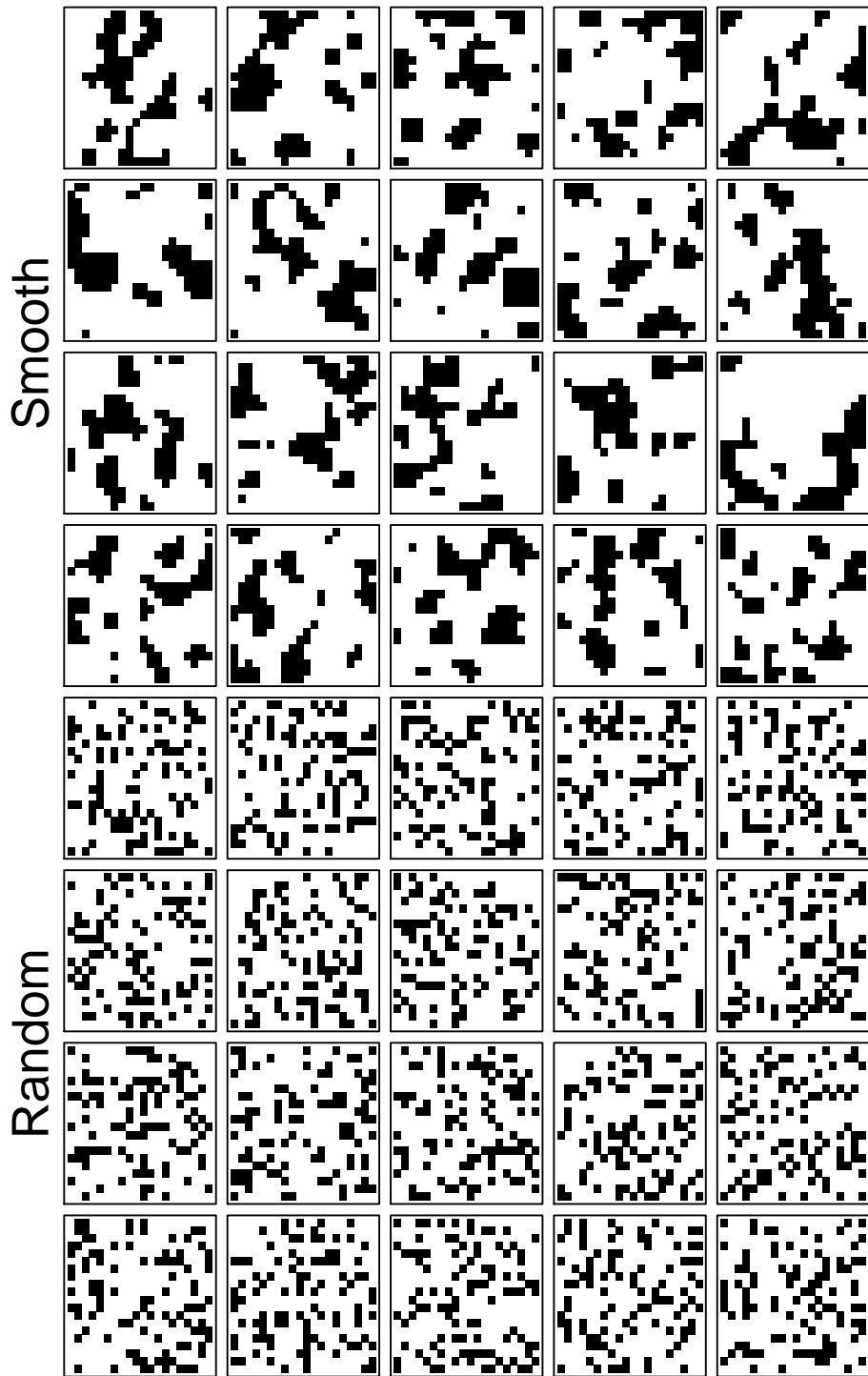


**Figure S14. Reward distributions used in the experiment.** Black squares represent blocks containing a reward, while white squares represent boxes containing no reward. Note that these plots omit the spacing between resource blocks in the experiment for readability.